Probing the Nonlinear Interactions of Supertidal Internal Waves Using a High-Resolution Regional Ocean Model

JOSEPH SKITKA,[a] BRIAN K. ARBIC,[a] RITABRATA THAKUR,[a] DIMITRIS MENEMENLIS,[b] WILLIAM R. PELTIER,[c] YULIN PAN,[d] KAYHAN MOMENI,[c] AND YUCHEN MA[c]

[a] *Department of Earth and Environmental Sciences, University of Michigan, Ann Arbor, Michigan*
[b] *Jet Propulsion Laboratory, California Institute of Technology, Pasadena, California*
[c] *Department of Physics, University of Toronto, Toronto, Ontario, Canada*
[d] *Department of Naval Architecture and Marine Engineering, University of Michigan, Ann Arbor, Michigan*

(Manuscript received 30 November 2022, in final form 26 September 2023, accepted 6 October 2023)

ABSTRACT: The internal wave (IW) continuum of a regional ocean model is studied in terms of the vertical spectral kinetic energy (KE) fluxes and transfers at high vertical wavenumbers. Previous work has shown that this model permits a partial representation of the IW cascade. In this work, vertical spectral KE flux is decomposed into catalyst, source, and destination vertical modes and frequency bands of nonlinear scattering, a framework that allows for the discernment of different types of nonlinear interactions involving both waves and eddies. Energy transfer within the supertidal IW continuum is found to be strongly dependent on resolution. Specifically, at a horizontal grid spacing of 1/48°, most KE in the supertidal continuum arrives there from lower-frequency modes through a single nonlinear interaction, whereas at 1/384° and with sufficient vertical resolution KE transfers within the supertidal IW continuum are comparable in size to KE transfer from lower-frequency modes. Additionally, comparisons are made with existing theoretical and observational work on energy pathways in the IW continuum. Induced diffusion (ID) is found to be associated with a weak forward frequency transfer within the supertidal IW continuum. ID is also limited to the highest vertical wavenumbers and is more sensitive to resolution relative to spectrally local interactions. At the same time, ID-like processes involving high-vertical-wavenumber near-inertial and tidal waves as well as low-vertical-wavenumber eddy fields are substantial, suggesting that the processes giving rise to a Garrett–Munk-like spectra in the present numerical simulation and perhaps the real ocean may be more varied than in idealized or wave-only frameworks.

KEYWORDS: Ocean; Internal waves; Regional models; Spectral analysis/models/distribution

1. Introduction

a. Motivation

Breaking internal gravity waves (IWs) are one of the most important processes underlying diapycnal mixing, which is thought to be a primary mechanism for closing and regulating the meridional overturning circulation (Wunsch and Ferrari 2004); in turn, the overturning circulation is a key regulator of the Earth system's climate (IPCC 2013). IW energy spectra are readily observable along one dimension in the ocean via dropped, floated, or dragged CTD probes and moored profilers (Alford et al. 2017). Phenomenological models of energy spectra associated with these observations were developed in the 1970s by Garrett and Munk (GM) (Garrett and Munk 1972, 1975, 1979), and theoretical models of the detailed dynamics that give rise to such spectra have been the subject of research in the ensuing decades (McComas 1977; Müller et al. 1986; Dematteis et al. 2022; Olbers 1976). The theoretical basis of IW dynamical processes inform state-of-the-art diapycnal mixing models [such as Internal Wave Dissipation, Energy and Mixing (IDEMIX); Olbers and Eden 2013; Eden and Olbers 2014] in global ocean simulations. However, verification of such theory via observations is difficult due to the intractability of rapidly measuring detailed two- or three-dimensional flow fields.

More recently, global (e.g., Arbic et al. 2010, 2018; Müller et al. 2015; Rocha et al. 2016b; Arbic 2022) and regional (e.g., Nelson et al. 2020; Pan et al. 2020; Thakur et al. 2022) ocean models have begun to permit detailed representations of the largest scales of the IW continuum due to a combination of tidal forcing, coupling to atmospheric wind and buoyancy forcing fields, and higher horizontal and vertical resolution (Arbic 2022). The highest-resolution regional models are able to permit detailed four-dimensional sampling of realistic supertidal internal wave fields (Thakur et al. 2022; Pan et al. 2020; Eden et al. 2020) that is not possible from observations, potentially a watershed breakthrough for IW modeling and theoretical innovation.

This paper will work to bring theoretical understanding of IW interactions into alignment with the internal wave dynamics as revealed in a high-resolution regional model using a novel asymmetric spectral flux decomposition [described in section 2b(2)]. It will also use both the spectral flux methods and numerical model output to interpret observations of spectral transfers that are made in fewer than three spatial dimensions, specifically in Sun and Pinkel (2012). A distinguishing feature of this work is that it will focus on the supertidal band of internal gravity waves and on interactions of internal waves with the mesoscale eddy field.

Denotes content that is immediately available upon publication as open access.

Corresponding author: Joseph Skitka, jskitka@umich.edu

DOI: 10.1175/JPO-D-22-0236.1

b. *Resonant nonlinear interactions in theoretical IW models*

The GM spectrum (Garrett and Munk 1975) does not attempt to describe the means of forcing, dissipation, spectral inhomogeneities due to tidal harmonics, or spatial inhomogeneities. It also is completely uninvolved with details of the nonlinear interactions that give rise to such a spectrum. McComas and Bretherton (1977) identified different types of nonlinear-interaction mechanisms likely to be important to the development of the IW continuum spectrum, including elastic scattering (ES), parametric subharmonic instability (PSI), and induced diffusion (ID). Dematteis and Lvov (2021) and Dematteis et al. (2022) provide a more restrictive definition of ID and introduce spectrally local interactions (LI) as an additional mechanism of consequence. This paper will focus on ID and, to a lesser extent, LI in part because they are most easily diagnosed from numerical model output with asymmetric spectral fluxes.

ID involves high-wavenumber, high-frequency waves scattering off of near-inertial, low-wavenumber waves and inducing diffusion of wave action, $\mathcal{A} = \mathrm{KE}/\omega_w$, forward in vertical wavenumber space. Here, ω_w denotes the modal frequency of waves in the flow, while ω will be reserved for the modal frequency of the entire flow including both waves and eddies. McComas and Bretherton (1977) found using two different theoretical methods that wave action should be conserved in the supertidal band under ID. The associated energy diffusion depends, then, on the direction of the frequency cascade. The direction of the frequency cascade, in turn, depends (through the dispersion relation) on the aspect ratio of the change in horizontal-to-vertical-wavenumber following the energy flow within the supertidal IW continuum through the interaction [see Fig. 5 in McComas and Müller (1981) and the pertinent discussion]. McComas (1977) argues that the horizontal wavenumber is approximately constant and therefore the associated frequency diffusion is backward and that some energy necessarily has to be moved into the near-inertial waves (NIWs) from the high-frequency IWs to conserve $\mathcal{A}$. On the other hand, Dematteis et al. (2022) argue that the horizontal wavenumber "keeps pace" with the vertical wavenumber, and therefore the associated frequency cascade is neutral-to-forward depending on the specific IW spectral slope. Therefore, the compensating energy will either be absent or will be exchanged from the near-inertial frequencies into the high frequencies.[1] The analysis of both McComas (1977) and Dematteis et al. (2022) assumes hydrostatic interactions, potentially complicating these pictures, although Dematteis et al. (2022) argue their findings are insensitive to the approximation.

This paper differentiates between such conflicting accounts of ID by decomposing the vertical[2] spectral kinetic energy flux into components based on the frequency band of the energy source. Vertical spectral fluxes are used because the various theoretical models of IW cascades are consistent in their predictions that within the IW "inertial range," energy flow is to smaller vertical wavenumbers (Müller et al. 1986; Dematteis et al. 2022). Our use of frequency-decomposed spectral fluxes also allows for the traditional definition of ID (which conserves and diffuses wave action in the supertidal band) to be decomposed into two components: 1) downscale kinetic energy diffusion within the supertidal band ($\mathrm{ID}_{\mathrm{diff}}$) and 2) the compensating energy exchanged with near-inertial and tidal frequencies ($\mathrm{ID}_{\mathrm{comp}}$). A separate but conceptually related mechanism, downscale kinetic energy diffusion that is induced by eddy fields instead of wave fields, is referred to as $\mathrm{ID}_{\mathrm{eddy}}$. Such labels are included here for reference, but they are not rigorously defined until section 2b(2).

c. *Observations of resonant nonlinear interactions*

Sun and Pinkel (2012) used sonar and CTD observations near Hawaii to directly quantify nonlinear energy transfers among supertidal internal waves. They found coherent energy transfers that were inconsistent with ID. We will label these energy transfers as a separate mechanism, "SP," throughout the paper but will hold off on discussing the physical meaning of this signal. They were also unable to find a signal where they expected to see ID on vertical-wavenumber bispectra. This paper produces a similar bispectrum in section 3b in an attempt to reproduce the most prominent feature from their observations while also explaining why Sun and Pinkel (2012) do not observe ID. In computing bispectra from model output, the assumption of Sun and Pinkel (2012) that the vertical-gradient component of the spectral KE transfer represents the entire transfer is tested.

d. *Resonant nonlinear interactions in IW-permitting simulations*

Regional models that permit a partially resolved IW continuum must account for significant spatial energy flux of IWs across the regional boundaries (Mazloff et al. 2020). Numerous regional models have a vigorous mesoscale eddy field but lack robust internal wave and internal tide forcing at the boundary conditions, (e.g., Nugroho et al. 2018; Renault et al. 2021; Wang et al. 2021). A straightforward means of accounting for this is to use IW-permitting global-model output to set the regional boundary conditions. Global models require simultaneous atmospheric

[1] Dematteis et al. (2022) use a specific set of parameters to define the IW spectrum that is consistent with the stationary solution of the wave-turbulence theory collision integral. For a frequency spectrum of $E(\omega) \sim \omega^{-2}$, their parameter choices imply a vertical wavenumber m energy spectrum that is $E(m) \sim m^{-2}$, which is not necessarily consistent with all parts of the ocean or the simulations in this paper (cf. with Fig. 4b). However, Dematteis et al. (2022) argue that it is necessary for this set of parameters to reflect dominant processes in the ocean so as to resolve the "oceanic ultraviolet catastrophe," i.e., for the spectral frequency fluxes associated with induced diffusion to be forward and not inverse given the lack of high-frequency energy sources to feed the IW continuum (Polzin and Lvov 2017). For this reason, we compare the present numerical simulations with predictions made for $E(m) \sim m^{-2}$ in Dematteis et al. (2022).

[2] A positive vertical spectral energy flux will denote energy transfer from low to high vertical wavenumber. The "vertical" strictly refers to the direction of the wavenumber of spectral modes; vertical spectral fluxes referenced in this paper therefore have no relation to hypothetical spectra computed from vertical spatial energy fluxes. This paper will sometimes drop the "energy" designation; e.g., "vertical spectral flux" implies a spectral flux of kinetic energy.

and tidal forcing as well as sufficient horizontal and vertical resolution in order to energize a robust IW field, conditions that have only begun to be implemented recently (Arbic et al. 2010; Müller et al. 2015; Rocha et al. 2016b,a; Arbic et al. 2018; Arbic 2022). Nelson et al. (2020), Pan et al. (2020), and Thakur et al. (2022) used a regional model with tidal and wind forcing, and, importantly, imposed IW forcing at the boundaries from an IW-permitting global model. These are the first and, along with two recent papers (Siyanbola et al. 2023; Delpech et al. 2023), are the only published regional models that attempt to resolve the IW boundary flux issue noted by Mazloff et al. (2020) at the time of submission. The present paper will continue using this approach.

Idealized simulations of flow realizations of the GM IW spectrum present an alternative approach for studying IW theory through numerical simulations. Eden et al. (2020) use this technique with a very fine 50-m horizontal grid spacing and are able to sidestep the problem of boundary conditions by diagnosing IW interactions on a periodic domain. They find PSI to be the dominant mechanism for moving energy from tidal frequencies in the range of $2f_0$–$2.5f_0$ (based on their Fig. 4c) and ID to play a relatively small role. This represents a promising approach of future study to which the asymmetric spectral fluxes of this paper could be applied.

As IW-permitting models adopt higher resolutions, they begin to resolve more of the IW continuum, both in global models (Müller et al. 2015; Savage et al. 2017) and regional models (Nelson et al. 2020). Pan et al. (2020) finds that IW dispersion curves in a high-resolution regional model are clearly defined over two orders of magnitude of frequency and horizontal wavenumbers, much greater than in available global models. They further find evidence for a dynamically significant ID in the IW continuum, which motivates the work of the present paper to study such dynamical processes.

High-resolution IW-permitting regional models now have the potential to validate recent advances in theoretical understanding and to study challenges faced in observations of internal wave scattering. Some open questions that we will address are:

- At what model resolutions do ID and LI become significant?
- Is ID associated with forward or inverse frequency cascade?
- How does $\mathrm{ID}_{\mathrm{diff}}$ compare to $\mathrm{ID}_{\mathrm{comp}}$?
- Why do Sun and Pinkel (2012) not see ID in their observations? What do they see?
- How important are $\mathrm{ID}_{\mathrm{eddy}}$ and other mechanisms that do not fit into existing categories of nonlinear wave–wave interactions?

2. Methods

a. The model

The numerical model simulates a region north of the Hawaiian archipelago (Fig. 1). It includes wind and astronomical forcing as well as rigidly imposed nested Dirichlet boundary conditions for all prognostic fields, which are provided from a similarly forced global ocean simulation of the Massachusetts Institute of Technology general circulation model (MITgcm), often denoted LLC4320 (Rocha et al. 2016b; Arbic et al. 2018).[3] As a result, it partially resolves the spectrum of near-inertial oscillations, internal tides and supertidal internal waves. The study area features a northward-propagating internal-tidal beam generated in the French Frigate Shoals as well as interactions with the Musician Seamounts. The region also features areas north and south of the critical latitude for PSI at 28.8°N (Alford et al. 2007). We use a hydrostatic formulation of MITgcm (Adcroft et al. 2015).

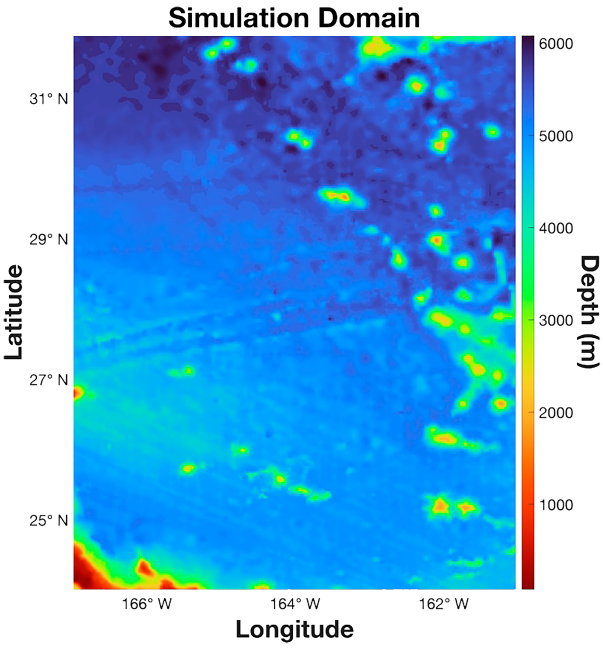

FIG. 1. Bathymetry of the region of study.

Previous work based on wavenumber and frequency spectra has demonstrated that this regional Hawaii simulation permits a partial representation of the internal wave cascade (Nelson et al. 2020; Pan et al. 2020; Thakur et al. 2022). Additionally, there is evidence that the model accurately represents the dispersion relation of the IWs, as indicated by the energy spectra in Fig. 8 of Pan et al. (2020). The mechanisms of wave damping in this model are the subject of ongoing research; most recently Thakur et al. (2022) found that the high-vertical-wavenumber end of the IW continuum is made more accurate by permitting greater energization at those scales. Despite having an incomplete picture of the exact details of IW damping, the general argument to be made here is that downscale spectral flux of IW KE will be in balance with damping at the highest vertical wavenumbers and will permit an approximately physically accurate picture of the nonlinear interactions at intermediate vertical wavenumbers. We do not explore spectral balance in horizontal wavenumber in this paper.

Another notable limitation of the model at representing IW dynamics is that it is hydrostatic. This will introduce error in the limit that $\omega \to N$, where N is the buoyancy frequency, and with

[3] Details of the boundary forcing are described in Nelson et al. (2020).

$\omega/N \gtrsim 1/2$ expected to be significant. As previous work with this model has done (Pan et al. 2020), we are not attempting to measure the interactions in this limit and we assume that the spectral energy transfer contributed at these frequencies is small. This can be justified as follows: supertidal nonlinear IW interactions in this numerical model are expected to predominantly occur in the pycnocline, where IW energy is largest (not shown) and $N > 20f_0$ [see Fig. 2 in Nelson et al. (2020)]. Here, f_0 denotes the Coriolis frequency at the central latitude of the regional domain. Nonlinear supertidal interactions diagnosed in this paper are dominated by $\omega < 10f_0$, so this assumption should be roughly reasonable for an initial study, even if the highest-frequency part of the continuum are restricted by resolution and damping. The use of nonhydrostatic models nonetheless can provide important details of the dynamics in the downscale limit that cannot be accessed in a model such as the one used in this paper (e.g., Eden et al. 2020).

The simulation employs a finite-volume solver. The horizontal eddy-viscosity scheme is a modified form of the Leith scheme (Fox-Kemper and Menemenlis 2008), while interior and mixed layer dissipation and diffusivity is handled by the κ-profile parameterization (KPP; Large et al. 1994). The Leith scheme and KPP are the dominant mechanisms acting in the ocean interior to dissipate KE in the modeled IW continuum. Wind forcing is updated every 6 h, while boundary conditions in the regional model are updated hourly. A staggered, second-order (explicit) Adams–Bashforth time-stepping method is used for all terms except the vertical viscosity (from the KPP scheme), which is treated implicitly using a backward time-stepping scheme. The model grid is stretched substantially in the vertical direction (vertical grid spacing is 0.333 m at the surface and 133 m at the domain bottom in the highest-resolution run). The regional model was run for 106 days, from 1 March 2012 until 15 June 2012, and output was collected every 20 min for the last 7 days of this period and used for the analysis presented in this work. The regional model was run with four different resolutions [the same ones as in Nelson et al. (2020)]:

1) 88 vertical levels and 2-km horizontal grid spacing,
2) 88 vertical levels and ~250-m horizontal grid spacing,
3) 264 vertical levels and 2-km horizontal grid spacing, and
4) 264 vertical levels and ~250-m horizontal grid spacing.

b. Spectral KE budgets

The present work is focused on attaining a picture of nonlinear IW triadic scattering mechanisms as far from spectrally inhomogeneous forcing as possible, that is, deep within the "inertial range" of the IW continuum. In particular, nonlinear interactions that are most active and easily discernible in this spectral range, ID and LI, will be diagnosed, while PSI and ES will not be. The strategy for attaining such a picture is to construct a partial spectral KE budget of terms that are expected to be dominant at mid-to-high vertical wavenumbers in the IW continuum: nonlinear fluxes, decomposed into contributions from different mechanisms based on frequency, and dissipation. This study will focus exclusively on KE. In future work, the asymmetric spectral flux methods used in this paper [see section 2b(2)] could be extended to apply to nonlinear scattering of buoyancy perturbations as well, thereby handling potential energy budgets.

The flow field is decomposed into spectral bands: the low-pass band (LP) with $\omega < 0.8f_0$, a bandpass of near-inertial and tidal frequencies (BP) with $0.8f_0 < \omega < 2.5f_0$, and a supertidal high-pass band (HP) with $2.5f_0 < \omega$. The HP band at high vertical wavenumber is of primary interest for the IW-continuum energetics. To the extent that an inertial range exists in the IW continuum, forcing and dissipation will exhibit scale separation and energy will move through the intermediate scales via nonlinear interactions among waves. The dissipation mechanisms and the vertical spectral flux should be in approximate balance at small scales. To compute these vertical spectral kinetic energy budgets, the velocity evolution due to each term in the governing equations must first be interpolated to a uniform vertical grid that has the same number of grid points. This sampling rate is based on numerical experiments with synthetic spectra.

The LP band includes both mesoscale eddies and the background time-mean flow. Because a mean flow is included in the flow solution and is not removed for analysis, IW frequencies are subject to Doppler shifting. The Doppler shift, if large, could affect the frequency analysis. However, in our regional model, this appears not to be the case–consider the following: In Pan et al. (2020) and Nelson et al. (2020), the dispersion relation and consistency relation of the IW field were studied, which agree with the relations caused only by waves and do not show obvious Doppler shift effects. When the Doppler shift is small, it can be considered as a small and random correction of the dispersion relation, under which a diffusion equation of wave action can be derived as in Savva and Vanneste (2018) and Dong et al. (2020). This diffusion effect is exactly what we studied in the paper (i.e., we have considered weak Doppler shift in our analysis.)

1) Terms and boundary conditions

Consider the horizontal velocity evolution equation

$$\partial_t \mathbf{u} = \underbrace{-(\mathbf{v}\cdot\nabla)\mathbf{u}}_{\mathsf{A}} \underbrace{-\nabla_h \frac{p}{\rho_0}}_{\mathsf{P}} \underbrace{-(\mathbf{f}\times\mathbf{u})_h}_{\mathsf{C}} + \mathsf{F} + \mathsf{D} + \mathrm{BCs} \quad (1)$$

with

$$\mathsf{D} = \mathsf{D}_{\mathrm{Leith}} + \mathsf{D}_{\mathrm{KPP\_ML}} + \mathsf{D}_{\mathrm{KPP\_Shear}} + \mathsf{D}_{\mathrm{KPP\_Conv}} + \mathsf{D}_{\mathrm{KPP\_BG}} + \mathsf{D}_{\mathrm{QBD}}, \quad (2)$$

where $\mathbf{u}$ is the 2D horizontal velocity vector, $\mathbf{v}$ is the 3D velocity vector, $\mathbf{f} = 2\Omega\sin(\theta)\hat{\mathbf{z}}$ is the Coriolis frequency vector, Ω is the frequency of Earth's rotation, θ is latitude, p is the combined hydrostatic and surface pressure, ρ_0 is the constant reference density, ∇_h is the 2D horizontal gradient operator, $()_h$ is the horizontal 2D component of the term within the parentheses, A is the advective term, P is the pressure term, F is forcing, D is dissipation, C is the Coriolis force, and BCs are spatial boundary forcing terms. Dissipation is decomposed into individual terms in Eq. (2). We are interested in terms and boundary conditions that may be active at small vertical scales. Under the assumption that the IW continuum acts as a

wave-turbulence cascade with scale separation between forcing and dissipation, the forcing terms will be ignored. Notes on the implementation of spectral diagnosis of the terms and boundary conditions of interest, which are computed for a partial vertical integrated spectral KE budget in section 2b(2), are listed in appendix E.

2) SPECTRAL FLUX AND TRANSFERS

Spectral-energy-flux methods can be used to study the direction of energy cascades across scales in ocean models and observations (e.g., Scott and Wang 2005; Schlösser and Eden 2007; Capet et al. 2008; Sun and Pinkel 2012; Arbic et al. 2013). This paper will utilize a decomposed version of the spectral energy fluxes and transfers that has some distinct benefits over previously used versions: the isolation of different spectral bands, a decomposition into interaction diagrams, and spatial resolution of the spectral exchanges in the direction orthogonal to the spectra computed [see section 2b(4)]. Also, while many other spectral methods, including implementations of wave-turbulence theory (WTT), spectral fluxes, and coarse-graining, often[4] consider energy exchange among sets of three modes (see appendix A), the spectral-flux decomposition presented in this paper will use an asymmetric version of scattering diagrams that isolates the exchange of energy between two modes mediated by a third mode, allowing for the direction and magnitude of energy exchange between any two scales to be exactly discerned.

To compute partial vertical spectral budgets, it is useful to write the horizontal velocity evolution [Eq. (1)] in terms of a generic sum of terms and boundary conditions:

$$\partial_t u_i = \sum_{\text{terms}} \partial_t (u_i)_{\text{terms}} \quad \text{and} \tag{3}$$

$$\partial_t (u_i)_{\mathsf{A}} = -v_j \partial_j u_i, \tag{4}$$

where u_i are the 2D horizontal velocity field components, v_j are the 3D velocity field components, subscripts sum over all applicable dimensions, and the summation runs over all terms and spatial boundary conditions (e.g., $\mathsf{D}_{\mathsf{KPP\_Shear}}$). The u_i and v_i are defined over coordinates $\{x, y, z, t\}$. The advective term A is explicitly written out as an important contribution to the horizontal velocity evolution in Eq. (4).

Local spectral budgets $\mathcal{T}_{\text{term}}$ are the change in KE of a specific spectral mode resulting from one of the terms in Eq. (3). The terminology is adopted from Scott and Arbic (2007), but others refer to this as a "spectral transfer function" (Arbic et al. 2014; Müller et al. 2015), a label that will be reserved strictly for the advective local spectral budget term, as discussed below. The strategy employed here is to represent the local spectral budget as a spatial integral so that integrated spectral budgets can be constructed out of them; this requires representing individual spectral modes in the position-space basis. The spatial-integral representations are preferred to purely spectral representations as they can be more efficiently computed from numerical model output. This can be written [see appendix C, including the extension to the hydrostatic approximation in Eq. (C12)]

$$\mathcal{T}_{\text{term},m_\alpha,\omega_\beta} = \left\langle \iint \sum_{\substack{\gamma=\pm\alpha \\ \lambda=\pm\beta}} \hat{u}_{i,m_\gamma,\omega_\lambda}(x, y) e^{2\pi \mathrm{i}(m_\gamma z - \omega_\lambda t)} \partial_t (u_i)_{\text{term}} \, dz \, dt \right\rangle, \tag{5}$$

where

$$\hat{u}_{i,m_\gamma,\omega_\lambda}(x, y) = \frac{1}{HT} \iint u_i(x, y, z, t) e^{-2\pi \mathrm{i}(m_\gamma z - \omega_\lambda t)} \, dz \, dt; \tag{6}$$

$$m_\gamma = \frac{\gamma}{H}; \quad \omega_\lambda = \frac{\lambda}{T}; \quad \text{and} \quad \alpha, \beta, \gamma, \lambda \in \mathbb{Z}. \tag{7}$$

Here, m_α are the discrete nonnegative vertical wavenumbers; when taken as an argument of $\mathcal{T}_{\text{term}}$ these vertical wavenumbers are restricted to be positive but can otherwise be negative. Also, ω_β now explicitly denotes a discrete frequency, H is the ocean depth, T is the duration of the time window being sampled, $\mathrm{i} = \sqrt{-1}$, $\mathbb{Z}$ is the set of all integers, and the angle brackets denote an average over horizontal space. In order for the position-space representation to be real-valued, positive and negative modes are paired together.[5] Note that $\mathcal{T}$ has dimensions of power/mass and would require an extra factor of (TH) to be scaled as a frequency–wavenumber density. One can integrate Eq. (5) to obtain contributions to the kinetic energy evolution at all vertical wavenumbers above a threshold. These "integrated spectral budget terms" (Scott and Arbic 2007) can be written as

$$\Pi^{>}_{\text{term},|m_\alpha|,\omega_\beta} = \left\langle \iint \sum_{\substack{|\gamma|>|\alpha| \\ |\lambda|>|\beta|}} \hat{u}_{i,m_\gamma,\omega_\lambda}(x, y) e^{2\pi \mathrm{i}(m_\gamma z - \omega_\lambda t)} \partial_t (u_i)_{\text{term}} \, dz \, dt \right\rangle. \tag{8}$$

As in Eq. (5), Eq. (8) includes both positive and negative valued wavenumbers and frequencies on the right-hand side so that the quantity being averaged over time and space is real-valued and $\Pi^{>}_{\text{term}}$ depends on the magnitude of vertical wavenumbers only. The integrated spectral budgets [Eq. (8)] will be used for evaluating the spectral flux integrated over bands of frequencies rather than individual frequencies.

The advective term conserves energy away from boundary effects on a divergence-less flow. Because of this, the local spectral budget contribution of advection is to simply transfer energy from one wavenumber to another. The contribution of

[4] One exception to this is a recent paper, Dematteis and Lvov (2023), that determines a realization of energy and wave-action exchanges between pairs of modes mediated by a third in the context of catalyst-source-symmetric WTT; see appendix A. The problem addressed in Dematteis and Lvov (2023) is similar to the one addressed with asymmetric spectral diagrams in this paper. Here we use symmetries evident in the governing equations to identify a realization of such energy exchanges. A comparison with and implications of using a catalyst-source symmetric system of equations to arrive at a realization of energy exchanges will not be explored in the present paper but offers a rich avenue of future enquiry.

[5] This follows from the requirement that $\hat{u}_{i,m_\alpha,\omega_\beta}(x, y) = \hat{u}^*_{i,-m_\alpha,-\omega_\beta}(x, y)$.

advection to the integrated spectral budget is a flux of KE between low wavenumbers and high wavenumbers. The local and integrated contributions from the advective term in particular are therefore referred to as spectral transfers and fluxes, respectively. These can be written out explicitly using Eqs. (5) and (8):

$$\mathcal{T}_{\mathsf{A},|m_\alpha|,\omega_\beta} = -\left\langle \iint \sum_{\substack{\gamma=\pm\alpha \\ \lambda=\pm\beta}} \hat{u}_{i,m_\gamma,\omega_\lambda}(x,y)e^{2\pi \mathrm{i}(m_\gamma z-\omega_\lambda t)}(v_j\partial_j u_i)\,dz\,dt \right\rangle$$

and (9)

$$\Pi^{>}_{\mathsf{A},|m_\alpha|,\omega_\beta} = -\left\langle \iint \sum_{\substack{|\gamma|>|\alpha| \\ |\lambda|>|\beta|}} \hat{u}_{i,m_\gamma,\omega_\lambda}(x,y)e^{2\pi \mathrm{i}(m_\gamma z-\omega_\lambda t)}(v_j\partial_j u_i)\,dz\,dt \right\rangle. \quad (10)$$

Note that if the frequency dependence is ignored by summing over all ω, then for an incompressible flow, for which $\partial_i v_i = 0$, Eq. (8) is equivalent to the form given by Frisch and Kolmogorov (1995) and Scott and Wang (2005),

$$\Pi^{>}_{\mathsf{A},|m_\alpha|} = -\left\langle \iint \left[\sum_{\substack{|\gamma|>|\alpha| \\ \text{all } \lambda}} \hat{u}_{i,m_\gamma,\omega_\lambda}(x,y)e^{2\pi \mathrm{i}(m_\gamma z-\omega_\lambda t)} \right] \times \left\{ v_j\partial_j \left[\sum_{\substack{|\gamma|<|\alpha| \\ \text{all } \lambda}} \hat{u}_{i,m_\gamma,\omega_\lambda}(x,y)e^{2\pi \mathrm{i}(m_\gamma z-\omega_\lambda t)} \right] \right\} dz\,dt \right\rangle. \quad (11)$$

For incompressible flows, the three velocity fields written in Eq. (10) can be organized into distinct roles that together constitute what we will label an "asymmetric diagram." In Eqs. (9) and (10), the advecting 3D field v_j acts as a "catalyst" and contributes no energy to the spectral flux. All KE transfer comes from the rightmost "source" u_i field, while the energy goes into the leftmost "destination" mode of $\hat{u}_{i,m_\gamma,\omega_\lambda}$, as shown in appendix A. These terms of catalyst, source, and destination modes will be used throughout the paper. Note that unlike the concept of a "triad" of modes, which represents a physical process involving all three modes that conserves energy, a diagram has a numerical value representing the change in energy in just one of the three modes catalyzed by just one of the remaining modes. By separating out these roles, we allow for the separation of KE flux between different frequency and/or wavenumber bands. For example, from Eq. (10):

$$\Pi^{>}_{\mathrm{LP}\xrightarrow{\mathrm{BP}}\mathrm{HP},\mathsf{A},|m_\alpha|} = -\left\langle \iint \sum_{\substack{|\gamma|>|\alpha| \\ \text{all } \lambda}} [\hat{u}^{\mathrm{HP}}_{i,m_\gamma,\omega_\lambda}(x,y)e^{2\pi \mathrm{i}(m_\gamma z-\omega_\lambda t)}](v_j^{\mathrm{BP}}\partial_j u_i^{\mathrm{LP}})\,dz\,dt \right\rangle \quad (12)$$

is the vertical spectral energy flux from the LP (eddy) frequencies scattering off the catalyst BP (tidal and near-inertial) frequencies into the HP (internal wave continuum) frequencies above a cutoff vertical wavenumber m_α. Here, $\hat{u}^{\mathrm{HP}}_{i,m_\gamma,\omega_\lambda}(x,y)$ refers to the spectral representation of a high-pass frequency filter acting on u_i, as defined at the beginning of this section 2b. Note that although $\hat{u}_i^{\mathrm{HP}}$ is written with an explicit dependence on ω, its amplitude will fall off rapidly outside of the applied frequency filter (in the case of HP, that would be $\omega < 2.5f_0$.) The average must be computed over the same time period used to define the frequency filter. Error is introduced from overlap of the bands, but it is determined to be small through numerical experiments. A 22%-tapered Tukey window is applied to the time series. The Tukey window also introduces error in the band isolation and reduces the magnitude of the transfers being computed. Through experiments with different window lengths, we determine that the findings of this paper are insensitive to errors arising from the Tukey window. Hereinafter, the A indicating the advective (or flux) terms will be dropped but implied for all Π and $\mathcal{T}$ that indicate directional KE exchange (e.g., $\mathrm{BP}\xrightarrow{\mathrm{all}}\mathrm{HP}$).

Induced diffusion interactions are generally defined as being sufficiently scale-separated between one IW mode and the other two in both frequency and wavenumber (McComas 1977), while local interactions have been used to describe interactions that are not scale separated in frequency and/or wavenumber (Dematteis et al. 2022). To associate spectral fluxes with such mechanisms, it is necessary to expand the source velocity field in Eq. (10):

$$\Pi^{>}_{\mathrm{HP}\xrightarrow{\mathrm{BP}}\mathrm{HP},|m_\alpha|} = -\left\langle \iint \sum_{\substack{|\gamma|>|\alpha| \\ \text{all } \lambda}} \sum_{\substack{\text{all } \eta \\ \text{all } \phi}} [\hat{u}^{\mathrm{HP}}_{i,m_\gamma^{\mathrm{dest}},\omega_\lambda}(x,y)e^{2\pi \mathrm{i}(m_\gamma z-\omega_\lambda t)}]v_j^{\mathrm{BP}}\partial_j[\hat{u}^{\mathrm{HP}}_{i,m_\eta^{\mathrm{src}},\omega_\phi}(x,y)e^{2\pi \mathrm{i}(m_\eta z-\omega_\phi t)}]\,dz\,dt \right\rangle \quad (13)$$

then, using the restriction that $m_{\mathrm{src}} + m_{\mathrm{cat}} = m_{\mathrm{dest}}$, this can be approximately decomposed into interactions that are scale separated such that the vertical wavenumbers of the source and destination fields are at least a factor of ξ larger than the catalyst field:

$$\Pi^{>}_{\mathrm{HP}\xrightarrow{\mathrm{BP}}\mathrm{HP},|m_\alpha|} = -\left\langle \iint \sum_{\substack{|\gamma|>|\alpha| \\ \text{all } \lambda}} \sum_{\substack{\frac{\min(|\eta|,|\gamma|)}{|\eta|-|\gamma|} \geq \xi \\ \text{all } \phi}} [\hat{u}^{\mathrm{HP}}_{i,m^{\mathrm{dest}}_\gamma,\omega_\lambda}(x,y)e^{2\pi i(m_\gamma z-\omega_\lambda t)}]v^{\mathrm{BP}}_j \partial_j [\hat{u}^{\mathrm{HP}}_{i,m^{\mathrm{src}}_\eta,\omega_\phi}(x,y)e^{2\pi i(m_\eta z-\omega_\phi t)}]\, dz\, dt \right\rangle$$
$$- \left\langle \iint \sum_{\substack{|\gamma|>|\alpha| \\ \text{all } \lambda}} \sum_{\substack{\frac{\min(|\eta|,|\gamma|)}{|\eta|-|\gamma|} < \xi \\ \text{all } \phi}} [\hat{u}^{\mathrm{HP}}_{i,m^{\mathrm{dest}}_\gamma,\omega_\lambda}(x,y)e^{2\pi i(m_\gamma z-\omega_\lambda t)}]v^{\mathrm{BP}}_j \partial_j [\hat{u}^{\mathrm{HP}}_{i,m^{\mathrm{src}}_\eta,\omega_\phi}(x,y)e^{2\pi i(m_\eta z-\omega_\phi t)}]\, dz\, dt \right\rangle. \quad (14)$$

Here, the first angle-bracketed term on the right-hand side indicates the scale-separated interactions that are associated with ID, whereas the interactions of the second angle-bracketed term are local in vertical wavenumber and are associated with LI. Note that the scale separation here is an approximation of that between the vertical wavenumber of the catalyst mode and the nearest source/destination mode, which we will refer to simply as "catalyst m-scale separated." The approximation uses only the magnitudes of the wavenumbers to compute their differences (e.g., $|\eta| - |\gamma|$ instead of $|\eta - \gamma|$). Along with the correct difference interactions such that $|m_{\mathrm{cat}}| = |m_{\mathrm{dest}}| - |m_{\mathrm{src}}|$, an erroneous class of additive interactions $|m_{\mathrm{cat}}| = |m_{\mathrm{dest}}| + |m_{\mathrm{src}}|$ is included in the approximate scale-separated form. These additive interactions are very weak and introduce only a small amount of error (computed and discussed in appendix F). This approximation allows for a much cheaper computation of the scale-separated spectral flux.

In the framework of Eq. (14), energy transfer into the supertidal (HP) band can then be decomposed:

$$\Pi^{>}_{\mathrm{all}\xrightarrow{}\mathrm{HP},|m_\alpha|} = \Pi^{>}_{\mathrm{ID}_{\mathrm{diff}}} + \Pi^{>}_{\mathrm{ID}_{\mathrm{comp}}} + \Pi^{>}_{\mathrm{SP}} + \Pi^{>}_{\mathrm{LI}} + \Pi^{>}_{\mathrm{ID}_{\mathrm{eddy}}} + \Pi_{\mathrm{BP}_{\mathrm{other}}} + \Pi_{\mathrm{LP}}, \quad (15)$$

where

$\Pi^{>}_{\mathrm{ID}_{\mathrm{diff}}}$ = "catalyst m-scale separated" $\Pi^{>}_{\mathrm{HP}\xrightarrow{\mathrm{BP}}\mathrm{HP},|m_\alpha|}$

$$= -\left\langle \iint \sum_{\substack{|\gamma|>|\alpha| \\ \text{all } \lambda}} \sum_{\substack{\frac{\min(|\eta|,|\gamma|)}{|\eta|-|\gamma|} \geq \xi \\ \text{all } \phi}} [\hat{u}^{\mathrm{HP}}_{i,m^{\mathrm{dest}}_\gamma,\omega_\lambda}(x,y)e^{2\pi \mathrm{i}(m_\gamma z-\omega_\lambda t)}]v^{\mathrm{BP}}_j \partial_j [\hat{u}^{\mathrm{HP}}_{i,m^{\mathrm{src}}_\eta,\omega_\phi}(x,y)e^{2\pi \mathrm{i}(m_\eta z-\omega_\phi t)}]\, dz\, dt \right\rangle, \quad (16)$$

$\Pi^{>}_{\mathrm{ID}_{\mathrm{comp}}}$ = "source m-scale separated" $\Pi^{>}_{\mathrm{BP}\xrightarrow{\mathrm{HP}}\mathrm{HP},|m_\alpha|}$

$$= -\left\langle \iint \sum_{\substack{|\gamma|>|\alpha| \\ \text{all } \lambda}} \sum_{\substack{\frac{\min(|\eta|-|\gamma|,|\gamma|)}{|\eta|} \geq \xi \\ \text{all } \phi}} [\hat{u}^{\mathrm{BP}}_{i,m^{\mathrm{dest}}_\gamma,\omega_\lambda}(x,y)e^{2\pi \mathrm{i}(m_\gamma z-\omega_\lambda t)}]\, v^{\mathrm{HP}}_j \partial_j [\hat{u}^{\mathrm{HP}}_{i,m^{\mathrm{src}}_\eta,\omega_\phi}(x,y)e^{2\pi \mathrm{i}(m_\eta z-\omega_\phi t)}]\, dz\, dt \right\rangle, \quad (17)$$

$\Pi^{>}_{\mathrm{SP}}$ = "source m-scale local" $\Pi^{>}_{\mathrm{BP}\xrightarrow{\mathrm{HP}}\mathrm{HP},|m_\alpha|}$

$$= -\left\langle \iint \sum_{\substack{|\gamma|>|\alpha| \\ \text{all } \lambda}} \sum_{\substack{\frac{\min(|\eta|-|\gamma|,|\gamma|)}{|\eta|} < \xi \\ \text{all } \phi}} [\hat{u}^{\mathrm{BP}}_{i,m^{\mathrm{dest}}_\gamma,\omega_\lambda}(x,y)e^{2\pi \mathrm{i}(m_\gamma z-\omega_\lambda t)}]v^{\mathrm{HP}}_j \partial_j [\hat{u}^{\mathrm{HP}}_{i,m^{\mathrm{src}}_\eta,\omega_\phi}(x,y)e^{2\pi \mathrm{i}(m_\eta z-\omega_\phi t)}]\, dz\, dt \right\rangle, \quad (18)$$

$\Pi^{>}_{\mathrm{LI}}$ = "catalyst m-scale local" $\Pi^{>}_{\mathrm{HP}\xrightarrow{\mathrm{BP}}\mathrm{HP},|m_\alpha|} + \Pi^{>}_{\mathrm{HP}\xrightarrow{\mathrm{HP}}\mathrm{HP},|m_\alpha|}$

$$= -\left\langle \iint \sum_{\substack{|\gamma|>|\alpha| \\ \text{all } \lambda}} \sum_{\substack{\frac{\min(|\eta|,|\gamma|)}{|\eta|-|\gamma|} < \xi \\ \text{all } \phi}} [\hat{u}^{\mathrm{HP}}_{i,m^{\mathrm{dest}}_\gamma,\omega_\lambda}(x,y)e^{2\pi \mathrm{i}(m_\gamma z-\omega_\lambda t)}]\, v^{\mathrm{BP}}_j \partial_j [\hat{u}^{\mathrm{HP}}_{i,m^{\mathrm{src}}_\eta,\omega_\phi}(x,y)e^{2\pi \mathrm{i}(m_\eta z-\omega_\phi t)}]\, dz\, dt \right\rangle$$
$$- \left\langle \iint \sum_{\substack{|\gamma|>|\alpha| \\ \text{all } \lambda}} \hat{u}^{\mathrm{HP}}_{i,m_\gamma,\omega_\lambda}(x,y)e^{2\pi \mathrm{i}(m_\gamma z-\omega_\lambda t)}(v^{\mathrm{HP}}_j \partial_j u^{\mathrm{HP}}_i)\, dz\, dt \right\rangle \quad (19)$$

$$\Pi^{>}_{\mathrm{ID_{eddy}}} = \Pi^{>}_{\mathrm{HP}\xrightarrow{\mathrm{LP}}\mathrm{HP},|m_\alpha|} = -\left\langle \iint \sum_{\substack{|\gamma|>|\alpha| \\ \text{all } \lambda}} \hat{u}^{\mathrm{HP}}_{i,m_\gamma,\omega_\lambda}(x,y) e^{2\pi \mathrm{i}(m_\gamma z-\omega_\lambda t)} (v^{\mathrm{LP}}_j \partial_j u^{\mathrm{HP}}_i)\, dz\, dt \right\rangle, \tag{20}$$

$$\Pi_{\mathrm{BP_{other}}} = \Pi^{>}_{\mathrm{BP}\xrightarrow{\mathrm{BP+LP}}\mathrm{HP},|m_\alpha|} = -\left\langle \iint \sum_{\substack{|\gamma|>|\alpha| \\ \text{all } \lambda}} \hat{u}^{\mathrm{HP}}_{i,m_\gamma,\omega_\lambda}(x,y) e^{2\pi \mathrm{i}(m_\gamma z-\omega_\lambda t)} (v^{\mathrm{BP+LP}}_j \partial_j u^{\mathrm{LP}}_i)\, dz\, dt \right\rangle, \tag{21}$$

and

$$\Pi_{\mathrm{LP}} = \Pi^{>}_{\mathrm{BP}\xrightarrow{\mathrm{all}}\mathrm{HP},|m_\alpha|} = -\left\langle \iint \sum_{\substack{|\gamma|>|\alpha| \\ \text{all } \lambda}} \hat{u}^{\mathrm{HP}}_{i,m_\gamma,\omega_\lambda}(x,y) e^{2\pi \mathrm{i}(m_\gamma z-\omega_\lambda t)} (v^{\mathrm{HP+BP+LP}}_j \partial_j u^{\mathrm{LP}}_i)\, dz\, dt \right\rangle. \tag{22}$$

The various spectral flux components, written Π_i, where i refers to different scattering mechanisms, and the different diagrams that constitute them are summarized in Fig. 2.

Induced diffusion, as it is described in McComas and Bretherton (1977), can be broken up into two subprocesses, $\mathrm{ID_{diff}}$ and $\mathrm{ID_{comp}}$. Each has a corresponding spectral flux: $\Pi_{\mathrm{ID}} = \Pi_{\mathrm{ID_{diff}}} + \Pi_{\mathrm{ID_{comp}}}$. The $\Pi_{\mathrm{ID_{diff}}}$ is the kinetic energy transfer within the supertidal band (HP) caused by scattering off the catalyst field of near-inertial and tidal waves (BP). The $\Pi_{\mathrm{ID_{comp}}}$ is the compensating energy transfer that must be exchanged between the near-inertial and tidal waves (BP) and the supertidal continuum (HP) in order to conserve supertidal wave action, as discussed in section 1b. The compensating energy diagrams for ($\mathrm{ID_{comp}}$) are related to the kinetic energy diffusion diagrams ($\mathrm{ID_{diff}}$) by an exchange of the catalyst and source modes, as depicted in Fig. 2. Both of these diagrams are treated together in wave turbulence theory because that theory (as it has been previously implemented) imposes symmetry between the source and catalyst modes, as discussed in appendix A and depicted in Fig. A3. Taken together, the two components of ID diffuse wave action in the supertidal band (but neither do this individually). Note that Π_{ID} is expected to diffuse wave action in the model evolution of the supertidal band only to the extent that scale separation exists between the catalyst modes and the source and destination modes, a rough approximation given our definition of ID.

Separately, one can consider KE diffusion that is induced by catalyst modes in the eddy field (LP) rather than the wave field (BP), which we label $\Pi_{\mathrm{ID_{eddy}}} = \Pi^{>}_{\mathrm{HP}\xrightarrow{\mathrm{LP}}\mathrm{HP},|m_\alpha|}$. On the other hand, Π_{LI} is the energy transfer into the supertidal band that is not scale-separated in either wavenumber or frequency. We approximate the latter possibility by supertidal modes that scatter off of other supertidal modes into the supertidal band, $\Pi^{>}_{\mathrm{HP}\xrightarrow{\mathrm{HP}}\mathrm{HP},|m_\alpha|}$. Together, Π_{LI}, $\Pi_{\mathrm{ID_{diff}}}$, and $\Pi_{\mathrm{ID_{eddy}}}$ constitute all of the energy transfer within (meaning coming from and remaining in) the supertidal band and represent a fully nonlinear inertial range. Other energy transfer into HP (coming from different frequency bands) is represented by $\Pi_{\mathrm{ID_{comp}}}$, Π_{SP}, $\Pi_{\mathrm{BP_{other}}} = \Pi^{>}_{\mathrm{BP}\xrightarrow{\mathrm{LP+BP}}\mathrm{HP},|m_\alpha|}$ and $\Pi_{\mathrm{LP}} = \Pi^{>}_{\mathrm{LP}\xrightarrow{\mathrm{all}}\mathrm{HP},|m_\alpha|}$. The Π_{SP} refers to a mechanisms observed in Sun and Pinkel (2012) that will be motivated in section 3d. ES primarily involves an exchange of energy between different upward and downward propagating waves rather than from scale to scale, so we do not expect to see Π_{ES} manifesting as downscale energy flux in this analysis. PSI would be contained in the spectral flux components that move energy from high frequency to half the frequency, catalyzed by half the frequency. Because BP contains tidal frequencies around $2f_0$ and near-inertial frequencies just above f_0, a positive (down-vertical-scale) signal should be included in $\Pi^{>}_{\mathrm{BP}\xrightarrow{\mathrm{BP}}\mathrm{BP},|m_\alpha|}$ while the decay of supertidal modes would show up in $\Pi^{>}_{\mathrm{HP}\xrightarrow{\mathrm{HP}}\mathrm{HP},|m_\alpha|}$ if the destination mode is still in the supertidal band, as well as positive values in $\Pi^{>}_{\mathrm{HP}\xrightarrow{\mathrm{BP}}\mathrm{BP},|m_\alpha|}$ and associated negative values under exchange of source and destination modes (see Fig. A2 in appendix A) in $\Pi^{>}_{\mathrm{BP}\xrightarrow{\mathrm{BP}}\mathrm{HP},|m_\alpha|}$ if the destination mode falls within the BP band. We do not attempt to separate out these terms as PSI is not a focus of this paper.

3) BISPECTRA

As with advective spectral fluxes in Eq. (13), advective spectral transfers [Eq. (9)] can also be written as a function of the vertical wavenumbers of two of the interacting fields instead of one. Such bispectra allow for the discernment of the spectral transfer as a function of specific catalyst and source modes, as well as the destination modes accessible from the single-wavenumber version in Eq. (9). As mentioned in section 1b, Sun and Pinkel (2012) computed observational bispectra and did not find an ID signal where they expected it. The bispectrum that they use can be written as

$$\tilde{\mathcal{B}}_{\mathrm{BP}\xrightarrow{\mathbf{HP}},m^{\mathrm{cat}}_\alpha,m^{\mathrm{dest}}_\beta} = 2\left\langle \sum_{\text{all } \eta,\phi,\sigma,\gamma} \mathrm{Re}(m^{\mathrm{src}}_\gamma \hat{u}^{\mathrm{HP}}_{i,m^{\mathrm{dest}}_\beta,\omega_\eta} \hat{v}^{\mathrm{HP}}_{3,m^{\mathrm{cat}}_\alpha,\omega_\phi} \hat{u}^{*\mathrm{BP}}_{i,m^{\mathrm{src}}_\gamma,\omega_\sigma}) \right\rangle. \tag{23}$$

Here, $\hat{v}_3$ is the vertical component of the spectral representation of the three-dimensional velocity field, which is defined as in Eq. (6) with $u_i \to v_i$ and $\hat{u}_i \to \hat{v}_i$. Additionally, the bold frequency-band labels indicate the two fields, in this case the catalyst and destination fields, that the independent wavenumbers reference. This form of the bispectrum neglects the horizontal gradients in the advective term as an approximation based on horizontal homogeneity in the flow, an assumption that is neither applicable nor theoretically correct (see section 3b). Computing such a bispectrum from three-dimensional data would be prohibitively computationally expensive. Therefore, we use a related form that is computed as an integral over position space:

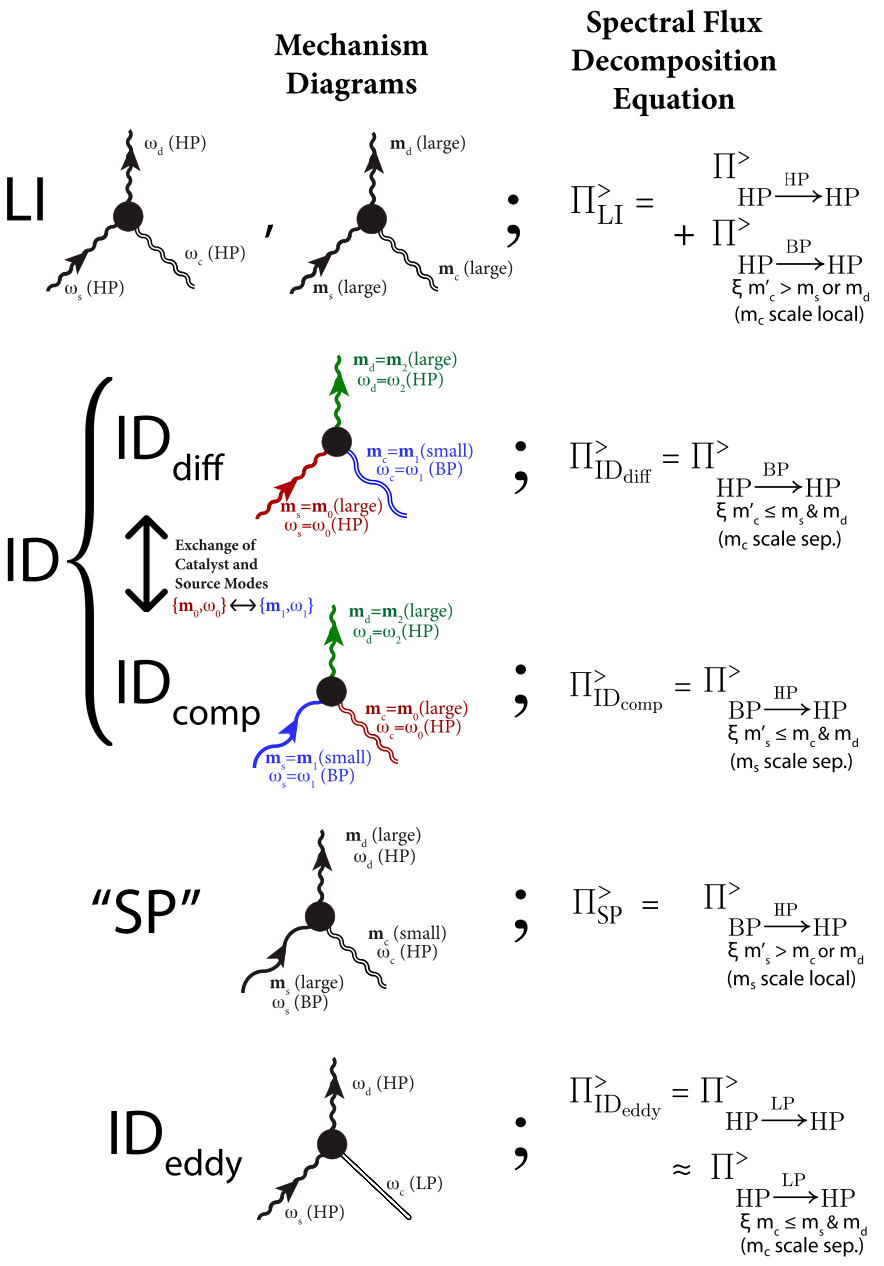

FIG. 2. Scattering diagrams, introduced in appendix A, for various mechanisms discussed in this paper. The left column shows the diagrams, and the right column gives the expression for the spectral flux $\Pi^{>}$ to which the diagrams contribute. Note that the prime notation in the right column, $|m_c'| = |m_d| - |m_s|$ and $|m_s'| = |m_d| - |m_c|$, indicates the approximation introduced in Eq. (14) and discussed in appendix F. SP refers to a mechanism that was observed by Sun and Pinkel (2012) and will be explained in the context of the results in section 3d. As described in appendix A, the bottom-left mode of each scattering diagram, m_s, is the source of KE in the diagram, the bottom-right mode, m_c, is the catalyst mode in the diagram and contributes no KE, and the top mode, m_d, is the destination of KE in the diagram. Therefore, each diagram represents the evolution of mode m_d and not the others. The line colors in the ID scattering diagrams each correspond to a specific mode—e.g., m_1, ω_1—to emphasize the exchange of catalyst and source modes.

$$\mathcal{B}_{\mathrm{BP}\xrightarrow{\mathrm{HP}}\mathbf{HP},|m_\alpha^{\mathrm{cat}}|,|m_\beta^{\mathrm{dest}}|} = -\left\langle \iint \sum_{\substack{\lambda=\pm\beta\\ \text{all }\phi}} \sum_{\substack{\gamma=\pm\alpha\\ \text{all }\eta}} e^{2\pi\mathrm{i}[(m_\gamma+m_\lambda)z-(\omega_\eta+\omega_\phi)t]} \hat{u}^{\mathrm{HP}}_{i,m_\lambda^{\mathrm{dest}},\omega_\phi}(x,y)\hat{v}^{\mathrm{HP}}_{j,m_\gamma^{\mathrm{cat}},\omega_\lambda}(x,y)\partial_j u_i^{\mathrm{BP}}(x,y,z,t)\,dz\,dt \right\rangle \tag{24}$$

One difference between Eq. (23) used by Sun and Pinkel (2012) and Eq. (24), used for this paper, is that, because the latter is computed in position space, the positive and negative signs of the wavenumbers cannot be separated. Thus, the bispectra computed with Eq. (24) are equivalent to those in which the positive- and negative-m_{cat} parts of Eq. (23) are averaged together. An implication of this averaging is that our bispectra will not pick up a signal from mechanisms that change sign with the sign of the wavenumber. For example, ES requires complex-valued modes to discern upward and downward propagating waves exchanging energy. The other key difference is that Sun and Pinkel (2012) are only able to use the vertical-gradient component in Eq. (23), whereas we have written our bispectra in Eq. (24) as containing both gradient directions unless stated otherwise.

Now that these bispectra have been defined, they can be interpreted along the same lines as the spectral flux decomposition in section 2b(2). Induced diffusion, as defined in McComas and Bretherton (1977), would be contained in $\mathcal{B}_{\mathrm{HP}\xrightarrow{\mathrm{BP}}\mathrm{HP}}$ and $\mathcal{B}_{\mathrm{BP}\xrightarrow{\mathrm{HP}}\mathrm{HP}}$, which contain the diffusion of wave energy in the supertidal band and the compensating energy delivered from BP, respectively. So, Sun and Pinkel's (2012) bispectrum [Eq. (23)] only captures $\mathrm{ID}_{\mathrm{comp}}$ and not the energy diffusion within the supertidal band. As previously mentioned, Dematteis et al. (2022) reason that in ID, the horizontal wavenumber should keep pace with the vertical in order to resolve the "oceanic ultraviolet catastrophe," implying a constant or forward frequency cascade, as opposed to an inverse cascade. Importantly, this means that compensating energy, and therefore induced diffusion, may not even be visible in the bispectra computed by Sun and Pinkel (2012) if the associated frequency cascade is neutral. In sections 2b(5) and 3c spectra transfers as a function of both frequency and vertical wavenumber are introduced and presented, respectively, that aim to identify the direction of the frequency cascade associated with ID and other processes. This will aid in interpreting $\mathcal{B}_{\mathrm{BP}\xrightarrow{\mathrm{HP}}\mathrm{HP}}$.

A likely reason that the bispectra of Sun and Pinkel (2012) was not identified by the authors as measuring $\mathrm{ID}_{\mathrm{comp}}$ is that in some versions of WTT the scattering coefficients are symmetric between the source and catalyst wavenumbers, as discussed in appendix A. The observations of Sun and Pinkel (2012) do not symmetrize between the catalyst and source modes, meaning these two bispectra may have actually been substantially different from one another and would not necessarily correspond to WTT predictions. Rather, they attempted to measure bispectra corresponding to $\mathcal{B}_{\mathrm{BP}\xrightarrow{\mathrm{HP}}\mathrm{HP}}$, which would imply a conceptual picture of energy compensation from the tidal, near-inertial, and subinertial frequencies into the IW continuum.

To address the question of whether the bispectra of Sun and Pinkel (2012) were consistent with the model output used in this paper, the catalyst bispectra, Eq. (24), is computed and presented in section 3d. However, in order to observe $\mathrm{ID}_{\mathrm{diff}}$, bispectra using the energy source rather than the catalyst mode are also computed. The latter formulation allows for the discernment of energy transfer between modes of similar wavenumber.[6] Such a source-destination bispectrum (containing $\mathrm{ID}_{\mathrm{diff}}$) can be written as

$$\mathcal{B}_{\mathbf{BP}\xrightarrow{\mathrm{HP}}\mathbf{HP},|m_\alpha^{\mathrm{src}}|,|m_\beta^{\mathrm{dest}}|} = -\left\langle \iint \sum_{\substack{\lambda=\pm\beta\\ \text{all }\phi}} \sum_{\substack{\gamma=\pm\alpha\\ \text{all }\eta}} [\hat{u}^{\mathrm{HP}}_{i,m_\lambda^{\mathrm{dest}},\omega_\phi}(x,y)e^{2\pi\mathrm{i}(m_\lambda z-\omega_\phi t)}]\, v_j^{\mathrm{HP}}\partial_j[\hat{u}^{\mathrm{BP}}_{i,m_\gamma^{\mathrm{src}},\omega_\eta}(x,y)e^{2\pi\mathrm{i}(m_\gamma z-\omega_\eta t)}]\,dz\,dt \right\rangle \tag{25}$$

4) Spatial distributions of integrated spectral budgets

The horizontal distributions of the vertical spectral flux [in Eq. (12)] can also be computed by omitting a horizontal average. The analogous component with horizontal spatial dependence looks like

$$\Pi^{>}_{\mathrm{ID}_{\mathrm{diff}},|m_\alpha|,\omega_\beta}(x,y) = -\iint \sum_{\substack{|\gamma|>|\alpha|\\ |\lambda|>|\beta|}} \hat{u}^{\mathrm{HP}}_{i,m_\gamma,\omega_\lambda}(x,y)e^{2\pi\mathrm{i}(m_\gamma z-\omega_\lambda t)} \times (v_j^{\mathrm{BP}}\partial_j u_i^{\mathrm{HP}})\,dz\,dt, \tag{26}$$

where now the parentheses indicate a vertical and time average. This will be used in Fig. 3 to select subregions of interest. Detailed comparison of spatial distributions of spectral flux as well as various dissipation mechanisms will be reserved for a future paper.

5) Spectral transfers versus wavenumber and frequency

As has been mentioned, compensating energy flux associated with induced diffusion ($\Pi_{\mathrm{ID}_{\mathrm{comp}}}$) may be forward, backward, or approximately zero depending on how the aspect ratio of the IW wavenumbers changes between the source and destination modes, which in turn corresponds to the direction of energy flow in frequency space through the IW dispersion relation. A

[6] If $\mathcal{B}_{\mathrm{HP}\xrightarrow{\mathrm{BP}}\mathrm{HP}}$ were instead plotted as a function of the catalyst mode [in the manner of Eq. (24)], the positive and negative catalyst modes would be expected to have oppositely signed bispectra. When the positive and negative catalyst-mode bispectra are averaged to generate a real-valued field to be integrated in position space [again, refer to Eq. (24)], the oppositely signed contributions would cancel.

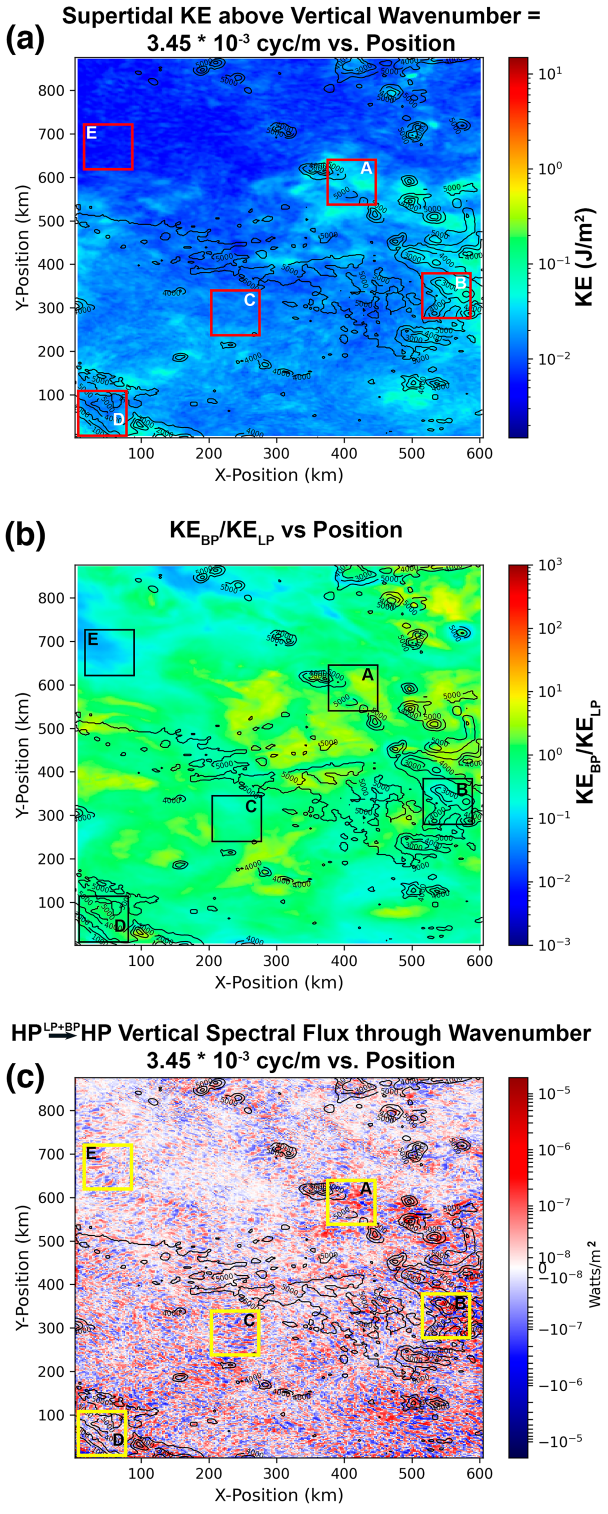

FIG. 3. Maps of various diagnostics in the regions of study: (a) supertidal (HP) kinetic energy above vertical wavenumber 3.45×10^{-3} m^{-1}, (b) the ratio of BP (sum of near-inertial and tidal) kinetic energy to LP (eddy) kinetic energy, and (c) downscale vertical induced-diffusion-type spectral kinetic energy flux through wavenumber 3.45×10^{-3} m^{-1}, computed as in Eq. (26). Contours indicate 1000-m levels of the bathymetry.

forward frequency cascade associated with induced diffusion within the supertidal band (i.e., specifically within $\Pi_{\mathrm{ID}_{\mathrm{diff}}}$) would require energy exchange from BP to HP ($\Pi_{\mathrm{ID}_{\mathrm{comp}}} > 0$) while an inverse frequency cascade would require energy exchange from HP to BP ($\Pi_{\mathrm{ID}_{\mathrm{comp}}} < 0.$). The direction of frequency exchange would be computationally prohibitive to determine directly. Therefore, we instead compute the spectral transfer as a function of destination vertical wavenumber and frequency:

$$\mathcal{T}_{\mathrm{HP}\xrightarrow{\mathrm{BP}}\mathrm{all},|m_\alpha|,\omega_\beta} = \left\langle \iint \sum_{\substack{\gamma=\pm\alpha \\ \lambda=\pm\beta}} e^{2\pi \mathrm{i}(m_\gamma z-\omega_\lambda t)} \hat{u}_{i,m_\gamma,\omega_\lambda}(x,y) v_j^{\mathrm{BP}} \partial_j (u_i)^{\mathrm{HP}}\, dz\, dt \right\rangle. \tag{27}$$

The transfer in Eq. (27) conserves energy in the supertidal band. Thus, it should be possible to infer the direction of the cascade by looking at where the sources and sinks of KE are in the HP band. Spectral transfers are also computed for the other terms in order to see, for example, if there is evidence of PSI, how energy is exchanged between potential and kinetic energy, and at what frequencies energy is entering and leaving the subdomains of interest.

3. Results and discussion

All results in this paper are computed from an average of five subregions of interest, shown in Fig. 3. Subregions, rather than the entire model domain, are used to compute results because of the prohibitive computational cost and data management requirements associated with the high-resolution case, which has 2.3 billion points of 3D data over the entire model domain. These subregions were chosen to capture a sample of rough and flat topography (visible in the contours) and a range of supertidal-frequency (HP) kinetic energies (Fig. 3a), supertidal (HP) vertical spectral kinetic energy fluxes (Fig. 3c), and ratios of near-inertial and tidal to eddy (BP/LP) kinetic energy (Fig. 3b). The five subregions in question were the only ones results were computed for. All results in this paper are computed with units of inverse volume as opposed to mass. We use a background density of $\rho_0 = 1027.5$ kg m^{-3}. When applicable, the domain-averaged Coriolis frequency, $f_0 = 6.85 \times 10^{-5}$ rad s^{-1} is also used. Also, on the basis of testing different values of ξ to define scale separation in ID, LI, and SP (appendix F), we choose to use $\xi = 2$.

The frequency spectrum of the high-resolution case (~250 m × 264 vertical levels) is shown in Fig. 4a with shading and separate curves indicating the three frequency bands discussed in section 2b. The band lines are shown at all frequencies to convey the overlap left after a 12th-order bandpass filter is applied. Nelson et al. (2020) have previously compared frequency spectra of these runs with observations and the GM spectrum (Garrett and Munk 1975). The supertidal frequency spectrum in the high-resolution simulation is slightly steeper than the asymptotic ω^{-2} prediction of GM while the spectrum from the low-resolution model (not shown) falls off much more steeply. In vertical wavenumber space (Fig. 4b), the eddy (LP) frequencies are energetically dominant at low and high wavenumbers while the BP frequencies are energetically dominant at intermediate wavenumbers. HP contains the least kinetic energy—an order of magnitude

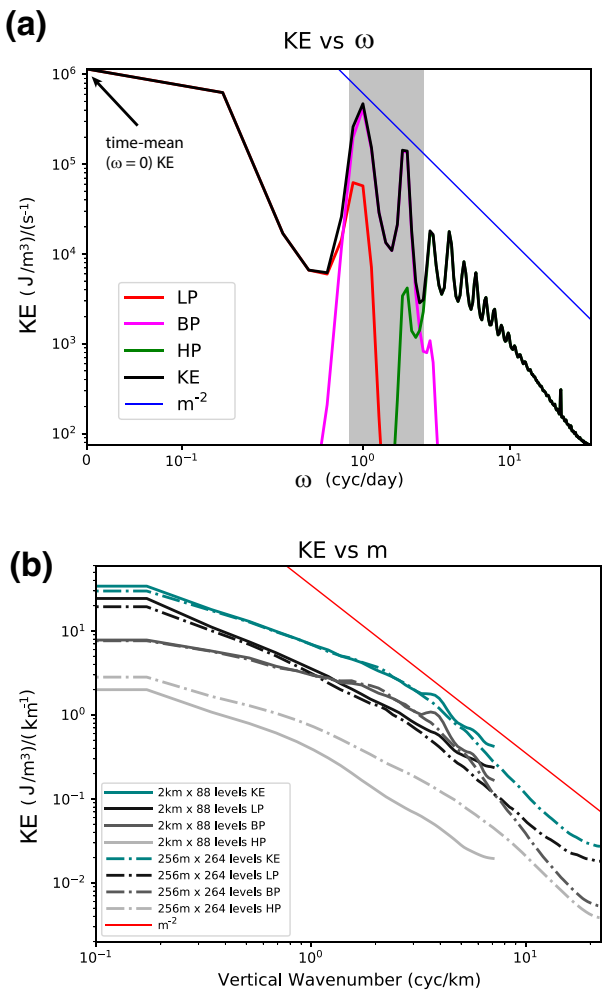

FIG. 4. (a) Frequency spectrum of the high-resolution case averaged across the subregions of interest, as displayed in Fig. 3. The band of $0.8f_0 < \omega < 2.5f_0$ is blocked out in gray. The low-pass/bandpass/high-pass decomposition (see text) of the overall frequency spectrum (black) is shown using the red, magenta, and green curves, respectively. The decomposition was performed using a 12th-order bandpass. The blue line indicates the asymptotic GM slope value of ω^{-2}. (b) Vertical-wavenumber spectrum of the different frequency bands in the high- and low-resolution cases averaged across the subregions of interest, as shown in Fig. 3.

less than BP. There is some energy buildup at the vertical grid-scale in both simulations in Fig. 4b. This buildup is likely a reflection of the sharp gradients that exist at the top and bottom of the domain and of the (intentional) choice to analyze the entire water column rather than tapering it, as is done in Thakur et al. (2022), Nelson et al. (2020), Pan et al. (2020). Finally, note that KE of the HP band is much greater at higher resolution, while the energy levels of BP and LP do not change very much between the different resolution cases.

a. Integrated vertical spectral KE budgets

As described in section 2b, the downscale vertical spectral KE flux and integrated vertical spectral dissipation transfers should be in balance at high vertical wavenumbers, at least to the extent that scale separation exists in the internal wave continuum. Assessing details of the budget at these wavenumbers is of primary importance. (In contrast, forcing terms are active at the lowest vertical wavenumbers such that the spectral flux and dissipation should not be in balance at those wavenumbers). To emphasize details at high wavenumbers, budgets are presented on linear axes as opposed to logarithmic axes, the latter of which would emphasize the lowest wavenumbers.

The partial integrated vertical spectral kinetic energy budget of the high-resolution case is shown in Fig. 5, with the left and right panels corresponding to all frequencies and HP frequencies. The overall amount of dissipation can be assessed by the value of the dissipation curve at $m = 0$, while the amount of energy that is dissipated at a given vertical wavenumber is proportional to the slope of the dissipation curve. The dissipation, spectral flux, and advection into the domain are in balance at the highest wavenumbers for both all frequencies (Fig. 5a) and the supertidal (Fig. 5b) frequencies. The latter indicates that the internal waves are energized at small and intermediate but not high vertical wavenumbers; energy in the IW field at high vertical wavenumbers gets there through nonlinear interactions among waves and eddies in the flow. This does not indicate that scale separation exists between forcing and dissipation; there is no classic inertial range at the resolutions used in this paper. However, the absence of forcing at the highest wavenumbers indicates that the IW continuum has some cascade-like properties and that an LES-type IW closure may be appropriate.

The frequency-decomposed vertical spectral KE-flux reflects specific types of nonlinear interactions that underlie the ocean's IW continuum. Within the HP band, $\mathrm{ID}_{\mathrm{diff}}$ and LI are expected to play a dominant role (Dematteis and Lvov 2021; Dematteis et al. 2022), at least among wave interactions. As described in section 2b(2), spectral flux into the HP band is decomposed into seven components [see Eq. (15) and Fig. 2]. These seven components are presented in Fig. 5b along with dissipation and boundary advection. The HP-to-HP-flux components are exchanges between large and small vertical scales on either side of vertical wavenumber m. On the other hand, the BP-to-HP and LP-to-HP flux components can come from any vertical wavenumber; these directional exchanges are depicted in wavenumber–frequency space in Fig. 6. Taken together, the components of the spectral flux shown in Figs. 5b and 6 constitute a complete decomposition of all advective energy exchange with supertidal (HP) modes above a given vertical wavenumber, m.

The individual components of spectral KE flux can be more easily compared across simulations and regions by looking at just a single vertical wavenumber. Integrated spectral budgets through a specific wavenumbers of $m = 3.8$ and $m = 12.5$ cycles per kilometer are compared across resolutions and subregions, respectively, in Fig. 7. The wavenumber of $m = 3.8$ cycles per kilometer was chosen to capture a strong signal from the nonlinear KE scattering mechanisms in both the high-resolution run (in which the peak Π_{LI} is at a slightly higher vertical wavenumber) and the low-resolution run (in which the peak Π_{LI} is at a slightly lower vertical wavenumber). In all cases,

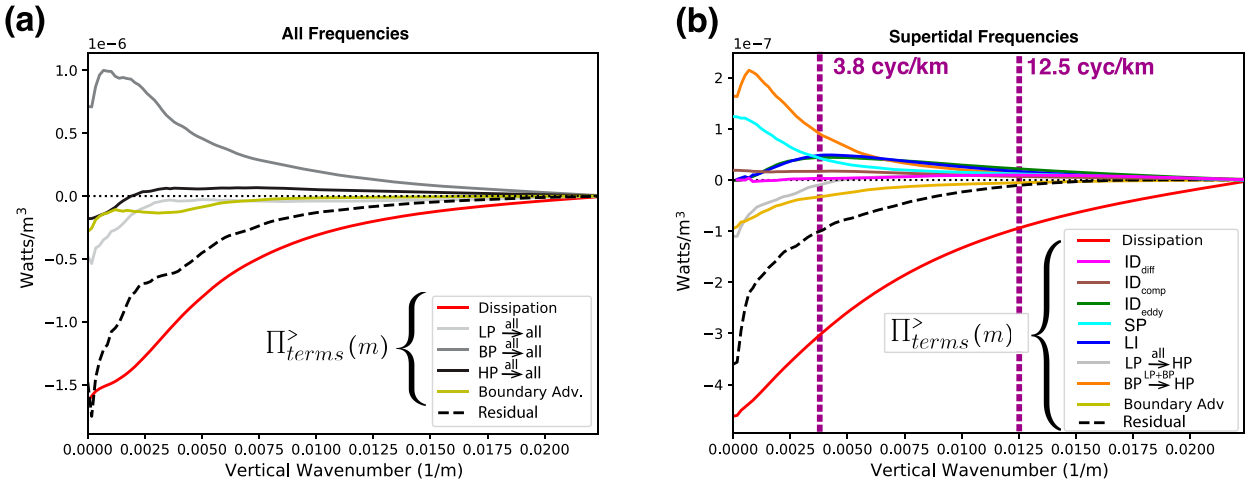

FIG. 5. Partial integrated spectral budgets of KE for the high-resolution run averaged across the subregions of interest, as shown in Fig. 3, for (a) all frequencies and (b) HP band ($\omega > 2.5f_0$). Note that the local spectral budget (the change in energy of a given wavenumber) is proportional to the slope of the curve at that wavenumber. The budget is "partial" because forcing terms and KPP mixed layer dissipation have been omitted from the analysis, such that the residual is only expected to be small at mid-to-high vertical wavenumbers. The purple lines indicate the vertical wavenumbers at which the terms are sampled for the resolution and subregional comparison in Fig. 7, described below.

BP-to-HP flux, which is decomposed into $\Pi_{ID_{comp}}$, Π_{SP}, and $\Pi_{BP_{other}}$, is the dominant advective energy transfer to the HP band relative to energy flux from the eddy (LP) and supertidal (HP) bands. Note that at higher vertical wavenumbers in the high-resolution case, the HP-to-HP flux becomes comparable to the BP-to-HP flux (seen in Fig. 5b), but this cannot be meaningfully compared with the lower resolutions that do not resolve such wavenumbers. The wavenumber of $m = 12.5$ cycles per kilometer was chosen for the regional comparison to maximize $\Pi_{ID_{diff}}$.

In all resolutions in Fig. 7, $\Pi_{ID_{diff}}$ is an insignificant portion of the vertical spectral KE flux through 3.8 cycles per meter, and intraband energy diffusion associated with Π_{LI} is only significant in the highest resolution case. For vertical spectral KE flux through 12.5 cycles per meter, which is only possible in the two cases with higher vertical resolution, Π_{LI} increases by a factor of ~50 and $\Pi_{ID_{diff}}$ increases by a factor of ~200 when the horizontal resolution is increased by a factor of 8. This highly nonlinear sensitivity suggests that ID and LI may change rapidly with further increases in horizontal resolution. This high sensitivity to horizontal resolution may be due to the requirement for high horizontal resolution to activate higher vertical modes in the continuum (Thakur et al. 2022).

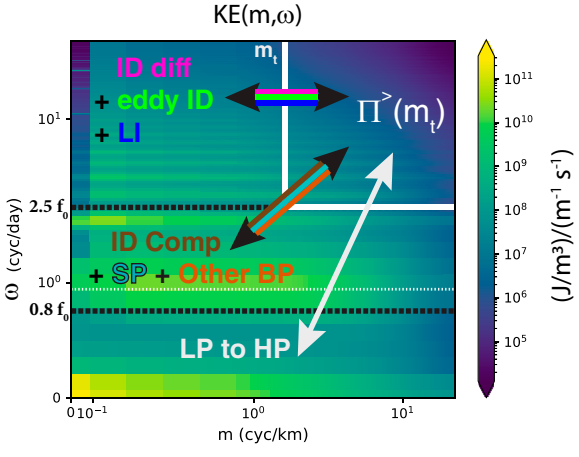

FIG. 6. The KE m–ω spectra and guide for different mechanisms averaged across the subregions of interest, as shown in Fig. 3. The white horizontal dotted line corresponds to the inertial frequency, f_0, averaged over the domain.

For vertical spectral KE flux through 12.5 cycles per meter in the high-resolution case, $\Pi_{ID_{comp}}$ is roughly one-half of the magnitude of $\Pi_{ID_{diff}}$ in all locations, suggesting that this component may be physically tied to supplying compensating energy to ensure conservation of wave action in the supertidal band, as hypothesized. This breaks down at smaller vertical wavenumbers and resolutions, at which $\Pi_{ID_{diff}}$ is negligible.

The decomposition in Fig. 7a indicates that the spectral flux due to eddy-induced diffusion ($\Pi_{ID_{eddy}} = \Pi^{>}_{HP \xrightarrow{LP} HP}$) is larger than both wave-induced energy diffusion ($\Pi_{ID_{diff}}$) and local interactions (Π_{LI}) in all cases except for the highest resolution case in which $\Pi_{ID_{eddy}}$ is comparable to $\Pi_{ID_{diff}} + \Pi_{LI}$. Perhaps a mechanistic understanding of the interactions that give rise to the GM spectrum cannot be gained without accounting for these eddy interactions, even though they are frequently omitted in wave-only frameworks of WTT.

Combined, the HP-to-HP spectral flux ($\Pi_{ID_{diff}}$, $\Pi_{ID_{eddy}}$ and Π_{LI}) contribute substantially (39% and 54% of the total downscale contributions to the integrated budget through 3.8 and 12.5 cycles per meter, respectively) for the cases with the highest resolution, and only modestly to the low horizontal and/or vertical resolution cases (≤25%). This trend is particularly pronounced in Π_{LI}, where it increases by a factor of ~5 with each successive resolution increase.

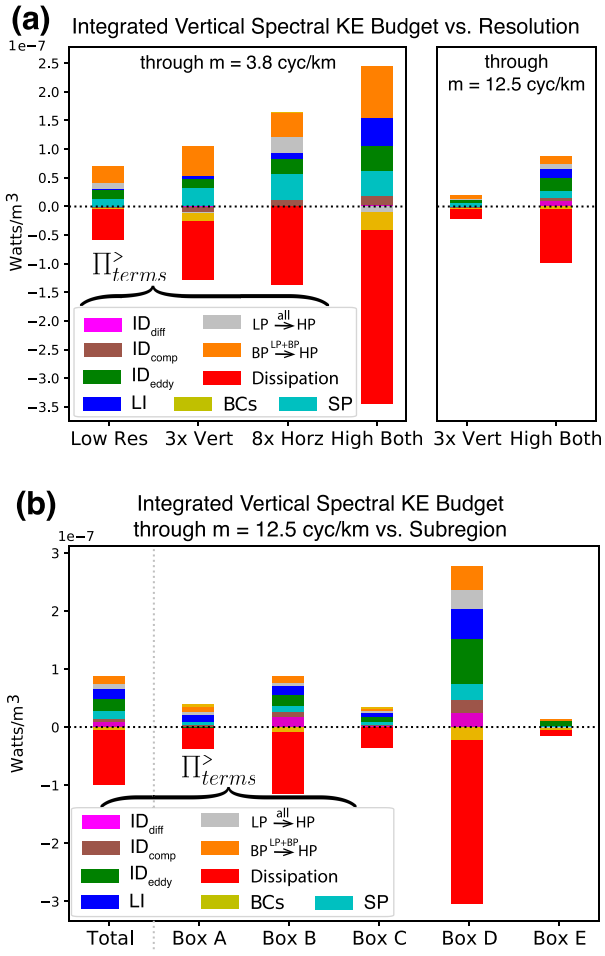

FIG. 7. A partial integrated vertical spectral KE budget [Eq. (12)] at supertidal (HP) frequencies (a) through 3.8 and 12.5 cycles per meter (indicated by a purple line in Fig. 5) vs resolution and (b) through 12.5 cycles per meter vs location in the high-resolution case. Spectral flux decomposition terms are included along with dissipation and boundary flux. Source terms and KPP's mixed layer dissipation are omitted. The PE-to-KE conversion is excluded but is confirmed to be small in these decompositions.

An important implication of the resolution dependence of HP-to-HP spectral flux is that at the lower resolutions (2 km × 88 levels, a resolution that is computationally feasible in an IW-permitting global model such as MITgcm LLC4320), the IW continuum will be approximately (generalized) quasilinear[7] (Marston et al. 2016) around the lower-frequency tides, near-inertial waves, and eddy fields in which interactions of the type $\Pi^{>}_{\mathrm{HP}\xrightarrow{\mathrm{all}}\mathrm{HP}}$ are not moving a substantial portion of the energy in the supertidal band. The quasilinear nature of the continuum in global models does not necessarily mean that their mixing and transport properties are inaccurate. In various turbulent flows, generalized quasilinear solutions can be useful approximations of the full nonlinear solutions, e.g., Marston et al. (2016). Nonetheless, the relative weakness of nonlinearity in the IW continuum in the new generation of global IW-permitting models should be accounted for when developing and applying closures and mixing schemes appropriate for such models. The use of higher resolutions in regional models permit a different, fully nonlinear regime of the IW continuum that 1) will be useful as a model of "truth" for understanding and improving IW handling in coarser resolution global models and 2) may also be optimally handled with a different dissipation mechanism that accounts for the different nature of the IW flows in regional versus global models.

The vertical spectral KE flux decomposition in the high-resolution case is compared across the different subregions in Fig. 7b. Boxes B and D, which are over rugged topography, clearly contribute the most to vertical spectral KE flux and dissipation of the five regions. In particular, both $\Pi_{\mathrm{ID}_{\mathrm{diff}}}$ and $\Pi_{\mathrm{ID}_{\mathrm{comp}}}$ are each larger in magnitude in boxes B and D than in the other boxes, while $\Pi_{\mathrm{ID}_{\mathrm{eddy}}}$ is largest in D. One possible reason for the markedly different breakdown of energy transfers in box D is its proximity to the domain boundary. This proximity would limit the amount of energy advecting into that region at the highest vertical wavenumbers and frequencies. Another possible reason is that the rough topography in box D is rather shallow, coming to within 150 m of the surface, whereas it is at great depth in box B (see Fig. 1). The latter reason would indicate enhanced flux (and wave-induced dissipation and mixing) occurring at depth through bottom interactions. Vertical distributions of horizontal spectral KE flux and dissipation mechanisms will be examined in a subsequent paper and will shed light on fluxes at depth.

The boxes (B and D) overlying rough topography also have negative contributions of HP KE to their budgets from the boundary advection (BC) term. Supertidal (HP) IW energy is generated in these regions and moves outward into the rest of the domain (such as boxes A and C).

b. *Bispectra of nonlinear scattering mechanisms*

Bispectra, introduced in Eq. (25) in section 2b(2), are displayed in Fig. 8. The $\mathcal{B}_{\mathrm{HP}\xrightarrow{\mathrm{BP}}\mathrm{HP}}$ (Fig. 8a) exhibits very clear downscale flux, with energy always leaving modes at smaller source vertical wavenumber than their destination wavenumber (indicated by the negative top-left half of the figure and positive in the bottom-right). Additionally, the strongest interactions occur near the diagonal, at which the source and destination wavenumbers are comparable. This is consistent with the two being separated by a small-wavenumber catalyst mode, as in the conceptual definition of ID (McComas and Bretherton 1977).

The $\mathcal{B}_{\mathrm{ID}_{\mathrm{eddy}}} = \mathcal{B}_{\mathrm{HP}\xrightarrow{\mathrm{LP}}\mathrm{HP}}$ (Fig. 8a) also exhibits very clear downscale flux, but in this case the catalyst modes are even smaller than in $\mathcal{B}_{\mathrm{HP}\xrightarrow{\mathrm{BP}}\mathrm{HP}}$, which contains $\mathrm{ID}_{\mathrm{diff}}$, as indicated by the tighter proximity to the positive and negative bands to the diagonal in Fig. 8b. This means that $\Pi_{\mathrm{ID}_{\mathrm{eddy}}}$ is strongly scale separated in wavenumber between the eddy mode and the wave modes, and interactions that are local in vertical wavenumber are not filtered out of $\Pi_{\mathrm{ID}_{\mathrm{eddy}}}$ for simplicity. Also apparent is a

[7] "Quasilinear" is a technical term that does not mean approximately linear.

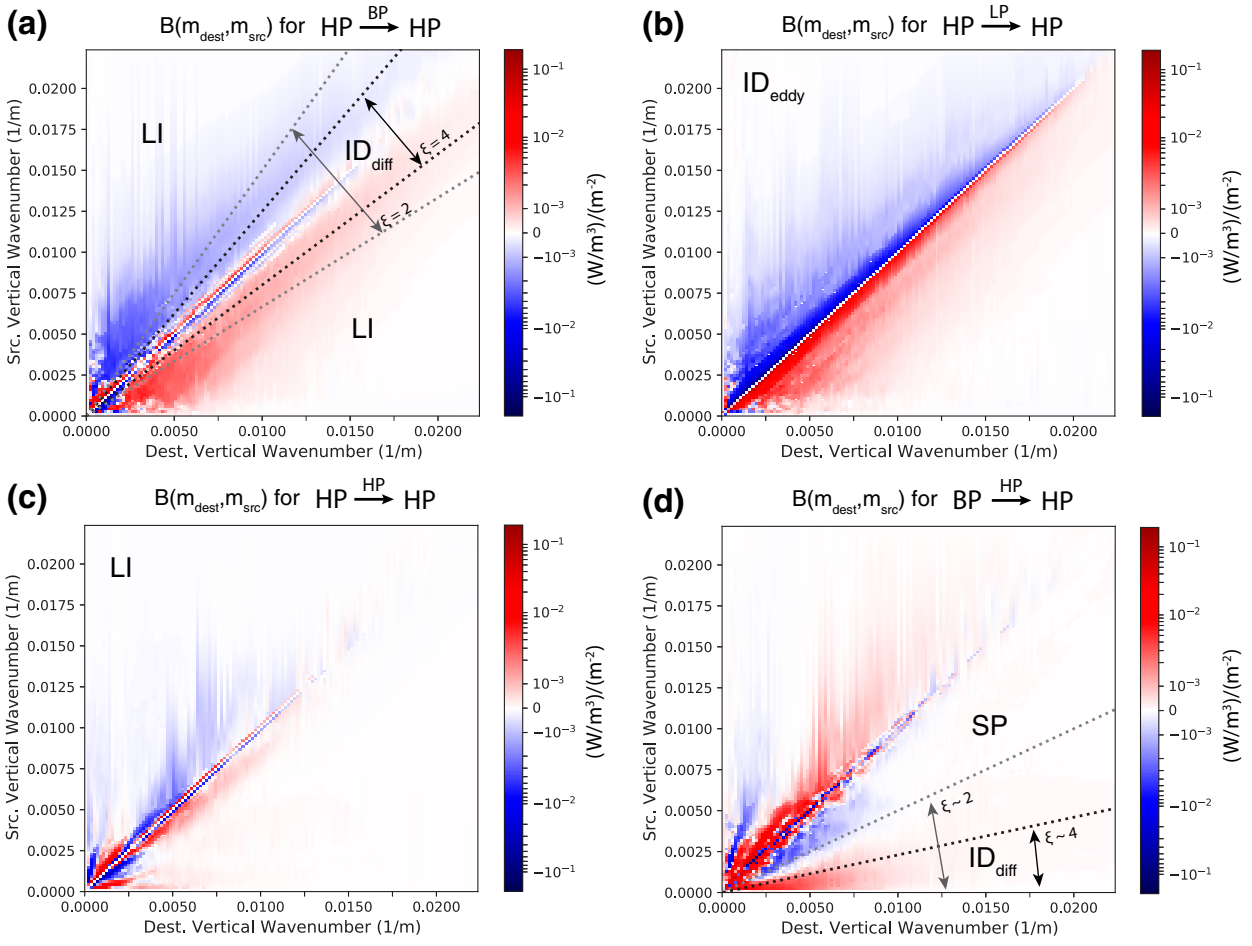

FIG. 8. Bispectra into the supertidal (HP) frequencies for the high-resolution case (case 4 in section 2a) averaged over the five regions of interest in Fig. 3. The bispectra displayed are (a) $\mathcal{B}_{\mathrm{HP}\xrightarrow{\mathrm{BP}}\mathrm{HP}}$, (b) $\mathcal{B}_{\mathrm{HP}\xrightarrow{\mathrm{LP}}\mathrm{HP}}$, (c) $\mathcal{B}_{\mathrm{HP}\xrightarrow{\mathrm{HP}}\mathrm{HP}}$, and (d) $\mathcal{B}_{\mathrm{BP}\xrightarrow{\mathrm{HP}}\mathrm{HP}}$. Bispectra are defined as the kinetic energy transfer from one vertical wavenumber to another, as defined in Eq. (25). The four contributions shown above constitute a complete decomposition; (d) is related to the bispectrum of Fig. 17 in Sun and Pinkel (2012) except that we use the KE source vertical wavenumber instead of the catalyst mode and we use both vertical and horizontal components of the gradient. The dotted lines indicate the partition of the spectral transfer into scale-separated and local components for different values of ξ. The partition of $\mathcal{B}_{\mathrm{BP}\xrightarrow{\mathrm{HP}}\mathrm{HP}}$ in (d) is plotted more accurately in Fig. 11b, below, as a function of the catalyst mode instead of the source mode.

thin line of upscale energy transfer hugging the diagonal in $\mathcal{B}_{\mathrm{HP}\xrightarrow{\mathrm{BP}}\mathrm{HP}}$ in Fig. 8a. When $\mathcal{B}_{\mathrm{HP}\xrightarrow{\mathrm{BP}}\mathrm{HP}}$ (Fig. 8a) and $\mathcal{B}_{\mathrm{HP}\xrightarrow{\mathrm{LP}}\mathrm{HP}}$ (Fig. 8b) are combined, they form continuous bands of downscale flux, meaning that the upscale flux occurring with small catalyst modes in $\mathcal{B}_{\mathrm{HP}\xrightarrow{\mathrm{BP}}\mathrm{HP}}$ is working against a larger downscale flux in $\mathcal{B}_{\mathrm{HP}\xrightarrow{\mathrm{LP}}\mathrm{HP}}$, effectively erasing it.

The bispectrum of $\mathcal{B}_{\mathrm{HP}\xrightarrow{\mathrm{HP}}\mathrm{HP}}$ (Fig. 8c) is generally much weaker than $\mathcal{B}_{\mathrm{HP}\xrightarrow{\mathrm{BP}}\mathrm{HP}}$. As with $\mathcal{B}_{\mathrm{HP}\xrightarrow{\mathrm{BP}}\mathrm{HP}}$, $\mathcal{B}_{\mathrm{HP}\xrightarrow{\mathrm{HP}}\mathrm{HP}}$ is strongest near the diagonal axis. Besides this, it exhibits polarity reversal as the wavenumbers increase along the diagonal axis, with several alternating antisymmetric bands of forward and backward spectral transfer. The strong signal along the diagonal reflects high-frequency, high-wavenumber IWs scattered by high-frequency and low-wavenumber IWs. Thus, the strongest interaction is only local in frequency and not vertical wavenumber. However, weaker signals off of the diagonal are present and reflect locality in both frequency and wavenumber.

The bispectra containing compensating energy, $\mathcal{B}_{\mathrm{BP}\xrightarrow{\mathrm{HP}}\mathrm{HP}}$, is shown in Fig. 8d. For a forward frequency cascade,[8] a positive signal is expected at small source wavenumbers and larger destination wavenumbers, as seen at the bottom of the plot. However, a positive signal is also seen along the diagonal. The positive signal corresponds to energy coming from high vertical wavenumbers in near-inertial and tidal frequencies (BP) scattering off of low-vertical-wavenumber modes in the supertidal band (HP), a mechanism that does not fit cleanly into existing wave interaction categories described in wave-turbulence approaches such as McComas and Bretherton (1977). However,

[8] The direction of the frequency cascade will be determined in section 3c.

Wagner and Young (2016) found a process through which near-inertial modes of high vertical wavenumber are energized through PSI, and perhaps these modes are acting in $\Pi^{>}_{\mathrm{ID}_{\mathrm{comp}}}$ diagrams in the present model. This mechanism, which we will label SP, will be discussed in greater detail in the context of the results of Sun and Pinkel (2012) in section 3d.

c. m–ω spectra

Two-dimensional wavenumber–frequency local spectral budgets, introduced in section 2b(5) are shown in Fig. 9. The primary motivation for computing these is to discern the direction of the frequency cascade associated with different nonlinear wave interactions. The advective spectra are decomposed in Figs. 9a–g. The energy transfer decomposition of the supertidal (HP) frequencies exists in the top portion of each figure, with $\omega > 2.5f_0$. Note that these spectra constitute a local (or transfer), as opposed to an integrated (or flux), budget. Also note that the plots for $\mathcal{T}_{\mathrm{HP}\xrightarrow{\mathrm{BP}}\mathrm{all}}$, $\mathcal{T}_{\mathrm{HP}\xrightarrow{\mathrm{LP}}\mathrm{all}}$ and $\mathcal{T}_{\mathrm{HP}\xrightarrow{\mathrm{HP}}\mathrm{all}}$ in Figs. 9a, 9b, and 9e, respectively, must conserve energy within the supertidal band, such that the positive and negative (blue and red) transfers above the $\omega = 2.5f_0$ line must be balanced.

For $\mathcal{T}_{\mathrm{HP}\xrightarrow{\mathrm{BP}}\mathrm{all}}$, transfers in the HP band increase along m and are approximately homogeneous in ω with a small sink at the lowest frequencies; this can be interpreted as moving energy predominantly from low to high vertical wavenumber, and slightly forward in frequency. This forward frequency cascade could be attributed to either ID or LI. To check if one is contributing more to the frequency cascade, we note that a forward frequency transfer is most apparent in boxes B and D, those with the roughest topography, while none is apparent in the other boxes (see Fig. 10). These are exactly the regions in which $\Pi_{\mathrm{ID}_{\mathrm{diff}}}$ is substantial, indicating the forward frequency cascade is likely due to ID, which is consistent with the argument of Dematteis et al. (2022) that the horizontal wavenumber "keeps pace" with the vertical wavenumber under induced diffusion. The computed spectral transfers are inconsistent with the theory of McComas and Müller (1981) in which ID is associated with an inverse-frequency cascade for supertidal IWs. It also means that compensating energy, $\Pi_{\mathrm{ID}_{\mathrm{comp}}}$, is expected to be weakly positive[9] in the present model results so as to conserve wave action among supertidal IWs.

The $\mathcal{T}_{\mathrm{HP}\xrightarrow{\mathrm{HP}}\mathrm{all}}$ (Fig. 9e), on the other hand, exhibits a clear forward frequency cascade at mid-to-high vertical wavenumber (indicated by KE leaving the lower frequencies in the HP band and entering the higher frequencies.) Although only a subset of LI, the forward direction of the frequency cascade of this component is consistent with the predictions of Dematteis et al. (2022) in which LI is expected to transfer energy more in the horizontal spectral direction relative to ID. LI should therefore have a more pronounced forward frequency transfer (see Fig. 6 in that paper), although Fig. 10 suggests this is only observed here in the component that is local in frequency as opposed to vertical wavenumber.

Energy transfer from BP (near-inertial and tidal frequencies) into HP (the supertidal band), depicted in Fig. 9c is positive throughout the HP band. Energy transfer from LP (eddy frequencies) into HP, depicted in Fig. 9d, shows some KE transfer from HP to LP at the lower vertical wavenumbers and only forward-frequency (LP-to-HP) transfer at the highest vertical wavenumbers. Note that in these two plots, the transfer need not sum to zero in the supertidal (HP) band.

KE advected into the regions of study is also decomposed into two-dimensional wavenumber–frequency spectra in Fig. 9f. This implies that, at least for the five subregions of interest, there is advection of supertidal KE into these regions at low-to-mid vertical wavenumber and advection out of these regions at high vertical wavenumbers.

Some theories of the IW continuum (e.g., McComas 1977) suggest that wind forcing injects energy at high ω, low m, at which point KE is moved through nonlinear interactions among waves to smaller ω. Signatures of this are not visible as an inverse frequency cascade at low vertical wavenumber in the advective spectra of transfer within the HP band (Figs. 9a,b,e), where KE might be leaving the highest frequencies. They are also not visible in the top left of the PE-to-KE conversion spectral, Fig. 9g, where some energy might be injected from SSH perturbations. These characteristics of the m–ω spectral transfers may be because wind forcing is limited to being updated only every 6 h. Higher-frequency forcing, or perhaps coupling to an atmospheric model, are likely necessary to force the flow in a manner consistent with the picture developed by McComas (1977) and will be explored in a future study. Such high-frequency forcing could also impact the overall direction of the ID or LI cascades that are observed. On the other hand, there is a PSI signal at tidal frequencies. The plot of KE transfer from BP (Fig. 9c) conserves energy within the BP band and the strong negative signal at low vertical wavenumber and the semidiurnal frequency is consistent with PSI. This likely PSI signal is about an order of magnitude lower in box E, which is north of the critical latitude for PSI, than in boxes B, C, and D, which are south of the critical latitude (not shown). The signal in box A, which straddles the critical latitude, is also much larger than in box E.

d. *Interpretation of and comparison with observations of Sun and Pinkel (2012)*

Sun and Pinkel (2012) use observational data to compute bispectra in an attempt to identify ID. Specifically, they compute bispectra using the catalyst mode and using only the vertical component of the gradient in the advective scattering [see Eq. (23)]. Related bispectra [Eq. (24)] are reproduced from the present model data (averaged over the 5 regions of

[9] To reprise some relevant points previously made in sections 1b and 2b(5), wave action is expected to be conserved in the supertidal band under ID. The definition of wave action, $A = E/\omega$, implies the direction of compensating energy that must be supplied from the catalyst band to conserve wave action is the same as that of the frequency cascade associated with ID, a point that is made clear in the discussion of Fig. 5 in McComas and Müller (1981). Dematteis et al. (2022) study spectra that they expect share properties with the real ocean that have both a weak forward frequency cascade (top row in Fig. 5 of that paper) and neutral frequency cascades (middle row in Fig. 5 of that paper) under ID, indicating compensating energy from the catalyst band to the supertidal band that is absent or weak.

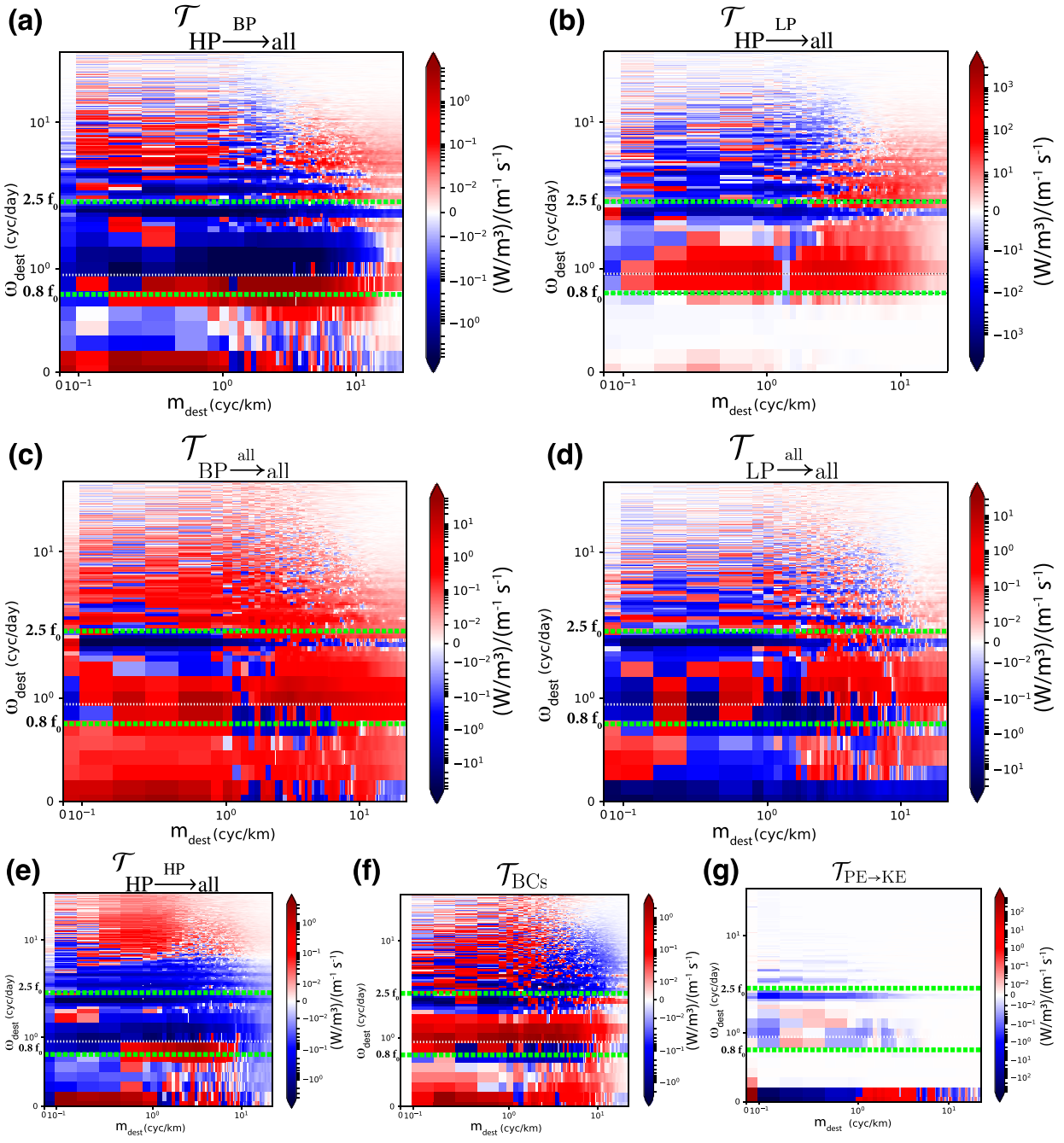

FIG. 9. The $m_{\mathrm{dest}} - \omega_{\mathrm{dest}}$ spectra of various local spectral budget terms [Eq. (27)] averaged across the subregions of interest, as shown in Fig. 3. The spectral transfers displayed are (a) $\mathcal{T}$: HP$\xrightarrow{\mathrm{BP}}$all, (b) $\mathcal{T}$: HP$\xrightarrow{\mathrm{LP}}$all, (c) $\mathcal{T}$: BP$\xrightarrow{\mathrm{all}}$all, (d) $\mathcal{T}$: LP$\xrightarrow{\mathrm{all}}$all, (e) $\mathcal{T}$: HP$\xrightarrow{\mathrm{HP}}$all, (f) $\mathcal{T}_{\mathrm{BCs}}$, and (g) $\mathcal{T}_{\mathrm{PE}\to\mathrm{KE}}$. The spectra are also averaged between positive and negative frequencies. The first five panels (a)–(e) constitute a complete decomposition of nonlinear advective scattering within any given frequency band. Note that the advective term is a spectral transfer as opposed to a spectral flux. Computing the flux would involve integrating the transfer in the wavenumber domain. The direction of frequency flux associated with a given transfer mechanism can be approximately discerned within a subspace that conserves energy under the evolution of that mechanism [e.g., in the HP band for $\mathcal{T}$: HP$\xrightarrow{\mathrm{BP}}$all in (a)]; if a sink (blue) is identified in the energy-conserving spectral band, energy must be transferred from those modes to the source (red) modes in that band. In this way, for example, the combined contributions of $\mathrm{ID}_{\mathrm{diff}}$ and LI to $\mathcal{T}$: HP$\xrightarrow{\mathrm{BP}}$HP in (a) can be seen to move KE from low to high ω.

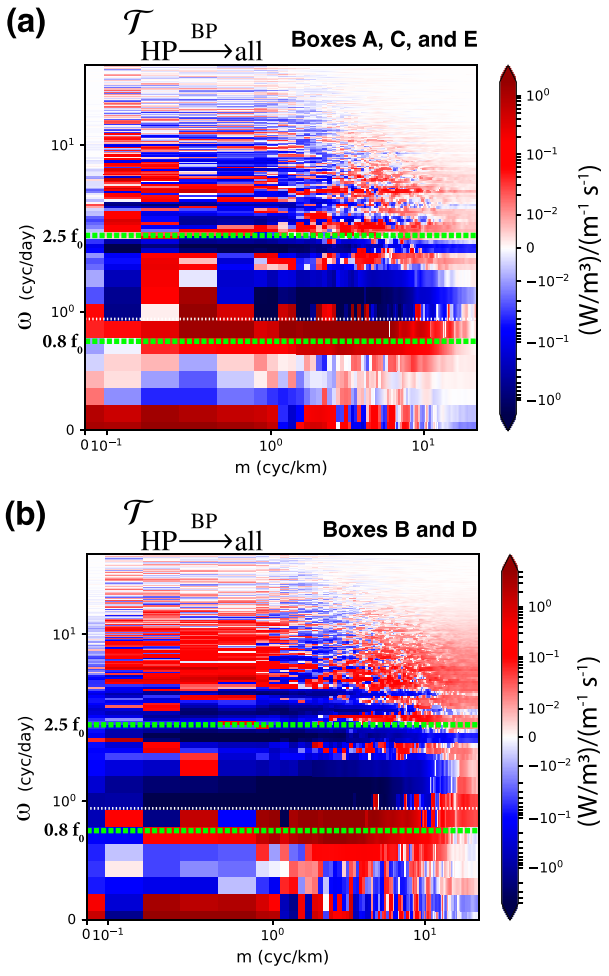

FIG. 10. Regional comparison of m–ω spectra for $\mathcal{T}_{\mathrm{HP}\longrightarrow\mathrm{all}}^{\mathrm{BP}}$ (as in Fig. 9a). Boxes B and D were selected for separate analysis because that is where most of the forward frequency cascade observable in the five boxes occurs, which is visible in the high-frequency part of the figures. In Fig. 7b, the ratio of $\Pi_{\mathrm{ID_{diff}}}$ to Π_{LI} is at least an order-of-magnitude greater in boxes B and D than in boxes A, C, and E. This suggests that $\Pi_{\mathrm{ID_{diff}}}$ is responsible for the forward frequency cascade seen in the HP band in Fig. 9a.

interest in the domain, depicted here in Fig. 3) in Fig. 11. To reiterate important points made in section 2b(3), an advantage of the method used in this paper is that unlike in Sun and Pinkel (2012), the bispectra can include the vertical and horizontal gradients (as in Fig. 11c). At the same time, the method used in this paper requires averaging over positive and negative values of the source and destination modes, implying that it cannot identify vertical anisotropies in scattering mechanisms such as through ES. Additionally, Sun and Pinkel (2012) separate their supertidal (HP) band from their low-pass background field (LP) by removing intermediate frequencies whereas the bispectra in Fig. 11 do not.

It is worth discussing whether it is appropriate to use only the vertical-gradient component of a bispectrum such as in Eq. (23). Sun and Pinkel (2012) point out that such an approximation is only valid in horizontally homogeneous flows and noted that would not be applicable in their region of study. We further point out that the horizontal-gradient part of these bispectra and advective tendencies in general should only be zero in horizontally homogeneous flows if the source and destination fields are the same [as it is in Gargett and Holloway (1984), which Sun and Pinkel (2012) cite to support their assumption]. To put this another way, if **f**, **g**, and **h** are distinct general incompressible three-dimensional velocity fields, then under horizontally homogeneous statistics, $\overline{\mathbf{f}\cdot[(\mathbf{g}\cdot\nabla_h)\mathbf{f}]}=0$ whereas $\overline{\mathbf{f}\cdot[(\mathbf{g}\cdot\nabla_h)\mathbf{h}]}\neq 0$, where the overbar indicates a time average and ∇_h is the horizontal gradient operator. In the compensating-energy bispectra used by Sun and Pinkel (2012), the source field is of near-inertial frequencies while the destination field is of supertidal frequencies. Thus, even in horizontally homogeneous flows, there will still be a nonzero value of these terms that represent the transfer of energy from low to high frequencies.

Sun and Pinkel's (2012) assumption that the horizontal-gradient contribution to the bispectra vanishes is also verified explicitly by comparing the bispectra with and without the horizontal-gradient contribution in Figs. 11a and 11b, respectively. We also compute the vertical- and horizontal-gradient spectral fluxes of $\Pi_{\mathrm{ID_{diff}}}$ in Fig. 11c. It is apparent that the assumption of small horizontal-gradient contribution is not valid in the present model output and care should be taken to devise alternative means to measure bispectra from observational data. A more realistic option may be to compare observational data of the vertical component with that of regional model output, such as this one, in an attempt to infer general features of the entire bispectra from the vertical component. This also suggests that we should be wary of attempts to interpret the bispectra features of Sun and Pinkel (2012) in the first place. Nonetheless, the general features of Fig. 11b are reflected in Fig. 11a. The inclusion of the horizontal gradients mostly shifts the signal in the positive direction. Therefore, with the aid of the computational results in Fig. 10, the features evident in the bispectra of Sun and Pinkel (2012) can still be interpreted.

Sun and Pinkel (2012) found a positive signal at $m_{\mathrm{cat}} \ll m_{\mathrm{dest}}$; this behavior is not expected from ID. Rather, a signal at $m_{\mathrm{cat}} \approx m_{\mathrm{dest}}$, which would be consistent with ID, was absent or very weak and not bicoherent. These features of Sun and Pinkel's (2012) results are generally consistent with the bispectra computed from the present model output in Fig. 11a, which also shows a strong positive signal at $m_{\mathrm{cat}} \ll m_{\mathrm{dest}}$, similar to Sun and Pinkel (2012). This signal indicates a transfer of energy from high-vertical-wavenumber near-inertial and tidal waves to high-vertical-wavenumber supertidal IWs via scattering off a low-vertical-wavenumber supertidal IWs. As this signal has been reproduced in the present numerical simulation, it is referred to as a distinct mechanism, SP, following the name of Sun and Pinkel. SP, occurring at $m_{\mathrm{cat}} \ll m_{\mathrm{dest}}$, reflects a transfer of energy from large vertical wavenumbers at near-inertial and tidal frequencies (BP) into supertidal modes at similar vertical wavenumbers (HP) via scattering off of catalyst modes of low vertical wavenumber in the supertidal band (HP). It is noteworthy that in Fig. 7b, in which $\Pi_{\mathrm{ID_{comp}}}$ shows a strong correspondence in

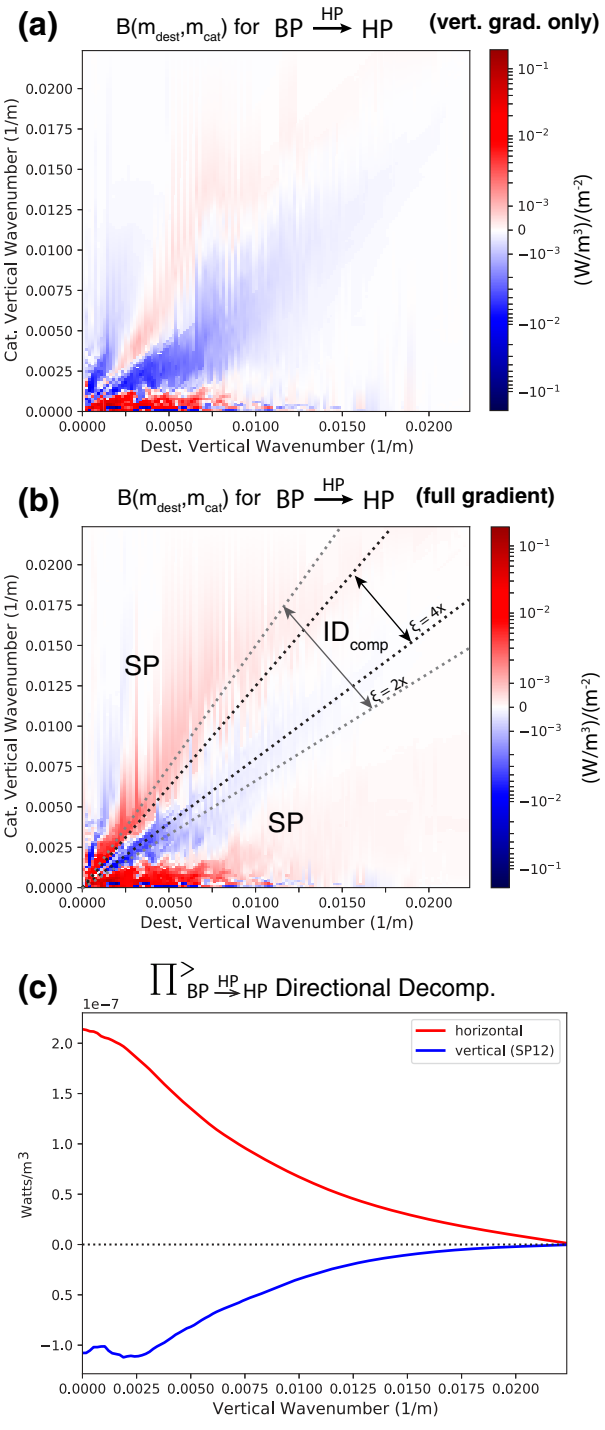

FIG. 11. The bispectra of the catalyst mode and destination wavenumber, as presented in Fig. 17 of Sun and Pinkel (2012) [see Eq. (24) in this paper]. (a) The bispectrum from Eq. (24) similar to that computed in Sun and Pinkel (2012, their Fig. 17). One key difference from Sun and Pinkel (2012) is that the contributions at the positive and negative vertical catalyst wavenumber are added together, making the bispectrum much easier to compute using 3D model output. This is computed as an average over the subregions of interest, as displayed in Fig. 3. (b) As in (a), but with the horizontal gradient magnitude $\Pi_{\mathrm{ID_{diff}}}$ over the subregions, Π_{SP} also shows a strong correspondence in magnitude to $\Pi_{\mathrm{ID_{diff}}}$. Perhaps SP is associated with ID through a mechanism that is of higher order (and involving more than one triadic scattering process). Alternatively, perhaps SP and ID are both correlated with rough topography.

The plots in Fig. 11a show a larger range of catalyst modes and a smaller range of destination modes than those in Sun and Pinkel (2012), thereby making the aspect ratio of $m_{\mathrm{cat}} \approx m_{\mathrm{dest}}$ easily identifiable as the diagonal. The bispectra of Sun and Pinkel (2012) are presented on a linear scale which makes it only easy to discern about one order of magnitude in their signal, possibly reflecting a observational noise floor. The present numerical results appear to have a lower noise floor (although we did not compute a bicoherence analysis.) The bispectra are presented on a log-scale color bar to reveal the weaker signal. The far left of the left panel of Fig. 16 in Sun and Pinkel (2012) shows alternating-signed bands near the origin. In Fig. 11a of this paper, a similar signal can be seen to extend weakly along the diagonal, $m_{\mathrm{cat}} \approx m_{\mathrm{dest}}$. This pattern should include $\mathrm{ID_{comp}}$ and indicates that compensating energy is primarily coming from modes that are catalysts in the associated $\mathrm{ID_{diff}}$ diagrams that are inducing KE diffusion downscale from this mode (positive above the diagonal) as opposed to from upscale into this mode (negative below the diagonal), which actually act weakly in the opposite direction.

4. Conclusions

With the increasing availability of high-resolution IW-permitting numerical models, wave-turbulence phenomenologists and theorists have acquired a validation tool capable of filling in gaps that are not easily accessible from observational data. At the same time, IW-permitting numerical models can enable more meaningful interpretation of observations, which are constrained by budgetary and other limitations from fully sampling complex four-dimensional IW fields. Another useful tool for these purposes is the asymmetric scattering diagram, which readily serves as a point of comparison with observations of triads [such as in Sun and Pinkel (2012)] and also allows for the study of resonant nonlinear mechanisms, such as induced diffusion and local interactions, that govern the IW cascade.

As a starting point, integrated vertical KE spectral budgets were computed for decomposition of both nonlinear advective scattering and dissipation. Advection and dissipation are found to be nearly in balance at high vertical wavenumbers, although an inertial range in which forcing and dissipation are absent was not present. Further results indicate that the extent of nonlinearity in such an IW continuum is highly dependent on the resolution of the model. In coarse 2 km resolutions (common in the highest-resolution global models), the IW continuum is approximately (generalized)

←
included. The dotted lines help to visualize the partition of the spectral transfer into scale-separated and local components for different values of ξ. (c) The integrated spectral KE flux from the vertical-gradient and horizontal-gradient contributions, thus highlighting their differences.

quasilinear around lower-frequency ($\omega < 2.5f_0$) background waves and eddies, meaning very little energy is transferred within the supertidal IW continuum. At such resolutions, most energy in the IW continuum has been transferred to a high-frequency mode from a low-frequency mode through a single nonlinear interaction rather than a series of cascade-like processes (such as through ID or LI). Thus, fully nonlinear aspects of the IW continuum are largely small in global models and at best can be parameterized based on available quasilinear flow information.

A central motivation of this work is to better understand nonlinear IW scattering mechanisms in a realistic ocean model. On one hand, theoretical questions in WTT pertaining to ID and LI in McComas and Bretherton (1977) and Dematteis et al. (2022) can be tested as well as decomposed using asymmetric spectral transfer diagrams. On the other hand, mechanisms that involve the eddy field or that do not fit neatly into existing frameworks can be measured, with the efficient computation of bispectra in position space being particularly instrumental for the latter activity. We find that ID is associated with a small forward frequency cascade and is strongest over rough topography. This stands in contrast to the theoretical framework of McComas and Müller (1981) who predicted an inverse frequency cascade associated with ID. Nonlinear spectral KE fluxes within the supertidal band involving only the wave part of the flow are also approximately decomposed into spectrally scale-separated (ID) and local (LI) components. The vast majority of these fluxes are local (LI) at low resolution. In addition, spectral fluxes are highly spatially inhomogeneous, and are largest within the subregion studied that had rough topography at depth.

The method of decomposing asymmetric spectral fluxes into catalyst, source, and destination modes enabled the separation of two distinct exchanges within ID: 1) $\mathrm{ID}_{\mathrm{diff}}$, the supertidal energy diffusion, and 2) $\mathrm{ID}_{\mathrm{comp}}$, energy compensation from the near-inertial and tidal frequencies. Partial spectral flux budgets reveal that $\Pi^{>}_{\mathrm{ID}_{\mathrm{comp}}}$ is similar in magnitude and varies subregionally with $\Pi^{>}_{\mathrm{ID}_{\mathrm{diff}}}$ at high vertical wavenumber. Using bispectra of asymmetric spectral KE transfers, a mechanism (termed SP) with a strong nonlinear energy exchange ($\Pi^{>}_{\mathrm{SP}}$) is identified both here and in the observational results of Sun and Pinkel (2012). This exchange moves KE from near-inertial and tidal frequencies of high vertical wavenumber into supertidal IWs of similar vertical wavenumber via scattering off of supertidal IWs that have lower vertical wavenumbers. Being an energy exchange from tidal and near-inertial frequencies to supertidal frequencies, SP is a key component of the generalized quasilinear dynamics that govern the IW continuum at low resolutions that would commonly be found in global models. SP does not fit into existing frameworks of nonlinear energy exchange among IWs, but perhaps this mechanism is real and important in the ocean given its presence in both Sun and Pinkel (2012) and this paper.

In addition, the vertical spectral KE flux of a mechanism analogous to $\mathrm{ID}_{\mathrm{diff}}$ in which eddy fields catalyze supertidal energy diffusion (termed $\Pi^{>}_{\mathrm{ID}_{\mathrm{eddy}}}$) is measured. $\Pi^{>}_{\mathrm{ID}_{\mathrm{eddy}}}$ is found to be much larger than $\Pi^{>}_{\mathrm{ID}_{\mathrm{diff}}}$ and $\Pi^{>}_{\mathrm{LI}}$ at lower resolutions and comparable to $\Pi^{>}_{\mathrm{ID}_{\mathrm{diff}}}$ and $\Pi^{>}_{\mathrm{LI}}$ only in the highest vertical and horizontal resolution simulation.

In summary, the present findings identify eddy-induced IW KE diffusion ($\Pi^{>}_{\mathrm{ID}_{\mathrm{eddy}}}$) as an important mechanism in shaping the IW spectrum in this simulation. SP [observed in Sun and Pinkel (2012)] is also found to be important in energizing the IW continuum in the present numerical simulation. Taken as a whole, the present results suggest internal wave interactions give rise to the GM spectrum in a way that differs from the idealized picture in many previous studies. This may be a reflection of the limited resolution or representation of IW dynamics. However, these findings can serve as a starting point for studying a more complete spectral budget of IW interactions that can be improved upon over time.

A natural next step will be to direct attention to dissipation mechanisms [building on Thakur et al. (2022)] and parameterizations of the IW continuum along with the spectral transfer decompositions presented in this paper. In particular, we will examine vertical and horizontal spatial distributions. This strategy will hopefully reveal different modeling strategies for quasilinear and fully nonlinear mechanisms that, in the real ocean, would move energy beyond the grid scale of a numerical model. Looking forward, we anticipate high-resolution regional models, such as this one, to become increasingly important in probing details of the IW cascade and potentially developing model parameterizations for such details.

Acknowledgments. Authors Skitka and Arbic acknowledge support from Office of Naval Research Grant N00014-19-1-2712. Authors Thakur and Arbic acknowledge support from National Science Foundation Grant OCE-1851164 and NASA Grant 80NSSC20K1135. We thank Cynthia Wu for insightful discussion of energy transfers among triads of modes. We thank both anonymous reviewers for improving the paper with helpful comments. For instance, one anonymous reviewer identified the point in the derivation of the kinetic equation of wave-turbulence theory in which symmetrization between the catalyst and source modes occurs, and the other anonymous reviewer encouraged us to apply scale separation in the vertical wavenumber to our definition of induced diffusion and related mechanisms.

Data availability statement. Data and data-processing scripts are publicly available online through Harvard Dataverse (https://doi.org/10.7910/DVN/FSMM1O; Skitka et al. 2022).

APPENDIX A

Asymmetric KE Transfer within Advective Triads

The exchange of energy among spectral modes of waves and eddies of different wavenumber in incompressible flow due to the advective nonlinearity can be understood in terms of triads of waves corresponding to source, catalyst, and destination modes of the kinetic energy. Start by expressing the advective term in the velocity field evolution in its incompressible flux form:

$$\partial_t v_i = -v_j \partial_j v_i, \tag{A1}$$

$$= -\partial_j (v_j v_i) + v_i \partial_j v_j, \tag{A2}$$

$$= -\partial_j (v_j v_i). \tag{A3}$$

Here, $v_i(x, y, z, t)$ is the ith component of the 3D velocity field and is a function of space and time, $\partial_t v_i$ denotes the velocity field evolution strictly due to the advective term, and subscripts are taken to imply a sum over dimensions. Equation (A3) follows from the divergence-less condition, $\partial_j v_j = 0$. This form will be substituted in the derivation below. Next, consider the domain-averaged change in KE in the horizontal velocity field from a single spectral component of the velocity field, $\tilde{v}_i(\mathbf{k}_0)$:

$$\frac{1}{2}\partial_t[\tilde{v}_i(\mathbf{k}_0)\tilde{v}_i^*(\mathbf{k}_0)] = \mathrm{Re}\{\tilde{v}_i(\mathbf{k}_0)\partial_t[\tilde{v}_i^*(\mathbf{k}_0)]\}. \tag{A4}$$

Here, $\mathbf{k}$ is the continuous 3D wavenumber (although solely horizontal or vertical may be used, the latter of which is done in the main part of this paper) and $\tilde{v}_i(\mathbf{k}_0)$ is the Fourier component of the velocity field, as defined on a continuous and infinite domain:

$$\tilde{v}_i(\mathbf{k}) = \int v_i(\mathbf{x}) e^{-2\pi \mathrm{i}(\mathbf{x}\cdot\mathbf{k})}\, d^3\mathbf{x}. \tag{A5}$$

Here, integrals are assumed to be from $-\infty$ to ∞ and each integral symbol represents a triple integral in 3D space. Also, note $v_i^*(\mathbf{k}) = v_i(-\mathbf{k})$. Then, making use of a form of the inverse Fourier transform corresponding to Eq. (A5),

$$v_i(\mathbf{x}) = \int \tilde{v}_i^*(\mathbf{k}) e^{-2\pi \mathrm{i}(\mathbf{x}\cdot\mathbf{k})}\, d^3\mathbf{k}, \tag{A6}$$

we can show

$$\frac{1}{2}\partial_t[\tilde{v}_i(\mathbf{k}_0)\tilde{v}_i^*(\mathbf{k}_0)] = \mathrm{Re}\{\tilde{v}_i(\mathbf{k}_0)\partial_t[\tilde{v}_i^*(\mathbf{k}_0)]\}, \tag{A7}$$

$$= \mathrm{Re}\{\tilde{v}_i(\mathbf{k}_0)\int -\partial_j[v_j(\mathbf{x})v_i(\mathbf{x})]e^{2\pi \mathrm{i}\mathbf{x}\cdot\mathbf{k}_0}\, d^3\mathbf{x}\}, \tag{A8}$$

$$= -\mathrm{Re}\left(\tilde{v}_i(\mathbf{k}_0)\int \partial_j\left\{\left[\int \tilde{v}_j^*(\mathbf{k}_1)e^{2\pi \mathrm{i}\mathbf{x}\cdot(-\mathbf{k}_1)}\, d^3\mathbf{k}_1\right]\left[\int \tilde{v}_i^*(\mathbf{k}_2)e^{2\pi \mathrm{i}\mathbf{x}\cdot(-\mathbf{k}_2)}\, d^3\mathbf{k}_2\right]\right\}(e^{2\pi \mathrm{i}\mathbf{x}\cdot\mathbf{k}_0})\, d^3\mathbf{x}\right), \tag{A9}$$

$$= -\mathrm{Re}\left\{\tilde{v}_i(\mathbf{k}_0)\iiint \tilde{v}_j^*(\mathbf{k}_1)\tilde{v}_i^*(\mathbf{k}_2)[-2\pi \mathrm{i}(\mathbf{k}_1 + \mathbf{k}_2)\cdot\hat{\mathbf{j}}][e^{-2\pi \mathrm{i}\mathbf{x}\cdot(\mathbf{k}_1+\mathbf{k}_2)}]\, d^3\mathbf{k}_1\, d^3\mathbf{k}_2(e^{2\pi \mathrm{i}\mathbf{x}\cdot\mathbf{k}_0})\, d^3\mathbf{x}\right\}, \tag{A10}$$

$$= 2\pi\, \mathrm{Re}\left\{\mathrm{i}\iint[(\mathbf{k}_1 + \mathbf{k}_2)\cdot\hat{\mathbf{j}}]\tilde{v}_i(\mathbf{k}_0)\tilde{v}_j^*(\mathbf{k}_1)\tilde{v}_i^*(\mathbf{k}_2)\delta^3(\mathbf{k}_0 - \mathbf{k}_1 - \mathbf{k}_2)\, d^3\mathbf{k}_1\, d^3\mathbf{k}_2\right\}, \tag{A11}$$

$$= 2\pi\, \mathrm{Re}\left[\mathrm{i}\int \overbrace{\underbrace{(\mathbf{k}_0\cdot\hat{\mathbf{j}})\tilde{v}_i(\mathbf{k}_0)}_{\text{Destination (Green)Arm}}\underbrace{\tilde{v}_j^*(\mathbf{k}_0 - \mathbf{k}_2)}_{\text{Catalyst (Blue)Arm}}\underbrace{\tilde{v}_i^*(\mathbf{k}_2)}_{\text{Source (Red)Arm}}}^{\text{Diagram in Fig. A1.}}\, d^3\mathbf{k}_2\right], \tag{A12}$$

where we have introduced $\hat{\mathbf{j}}$ as the unit vector in the spatial dimension corresponding to index j. The integrand of this equation can be symbolically represented as a diagram as in Figs. A1–A3. In Eq. (A12), the labeled parts correspond to the different arms of the scattering diagram in Fig. A1. Each of the diagrams in Eq. (A12) represents the change in energy in just one mode, $\mathbf{k}_0$. To represent an exchange of energy from one mode to another, we must consider pairs of triads. Because the advective nonlinearity conserves energy in an incompressible flow, the simplest scenario is for the value of the diagram (representing the integral quantity of kinetic energy change of the mode $\mathbf{k}_0$) to be opposite under the exchange of $\mathbf{k}_0 \leftrightarrow \mathbf{k}_2$ and that this holds for all $d^3\mathbf{k}_2$ and $d^3\mathbf{k}_0$ in their respective integrands. To verify this, write the flux with these modes exchanged:

$$\frac{1}{2}\partial_t[\tilde{v}_i(\mathbf{k}_2)\tilde{v}_i^*(\mathbf{k}_2)]$$

$$= 2\pi\, \mathrm{Re}\left[\mathrm{i}\int(\mathbf{k}_2\cdot\hat{\mathbf{j}})\tilde{v}_i(\mathbf{k}_2)\tilde{v}_j^*(\mathbf{k}_2 - \mathbf{k}_0)\tilde{v}_i^*(\mathbf{k}_0)\, d^3\mathbf{k}_0\right], \tag{A13}$$

$$= 2\pi\, \mathrm{Re}\left[\mathrm{i}\int(\mathbf{k}_2\cdot\hat{\mathbf{j}})\tilde{v}_i(\mathbf{k}_2)\tilde{v}_j(\mathbf{k}_0 - \mathbf{k}_2)\tilde{v}_i^*(\mathbf{k}_0)\, d^3\mathbf{k}_0\right]. \tag{A14}$$

Invoking the divergence-free condition for a general mode $\mathbf{k}$:

$$0 = \partial_j v_j(\mathbf{x}), \tag{A15}$$

$$= \int \partial_j\tilde{v}_j(\mathbf{k})e^{-2\pi \mathrm{i}\mathbf{x}\cdot\mathbf{k}}\, d^3\mathbf{x}_0, \tag{A16}$$

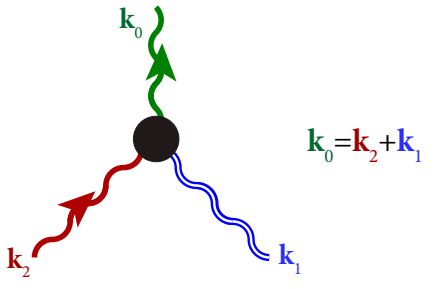

FIG. A1. An advective scattering diagram from the integrand of Eq. (A12). The arrows indicate the direction of kinetic energy flow. Here, $\mathbf{k}_0$ refers to the destination mode of KE, $\mathbf{k}_2$ is the source mode of KE, and $\mathbf{k}_1$ is the catalyst mode that neither contributes nor receives KE. This diagram represents the change in KE in the destination mode, $\mathbf{k}_2$, only, such that pairs of diagrams are required to represent an exchange of energy between modes, as displayed in Fig. A2, below.

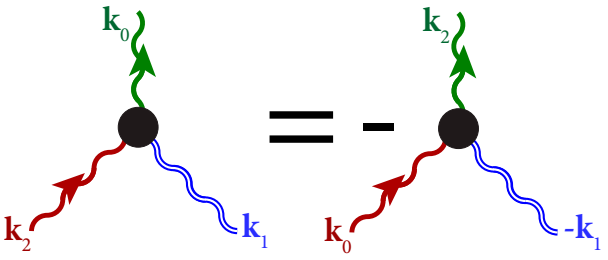

FIG. A2. Energy conservation is expressed through a pair of oppositely signed diagrams corresponding to the removal of energy from one mode and the injection of energy from another. Note that a diagram is distinct from the concept of a triad in that a single triad represents all exchanges of energy among three modes and does not correspond to a single physical quantity, whereas a diagram does correspond to a single quantity.

$$= -\int 2\pi \mathrm{i}(\mathbf{k}\cdot\hat{\mathbf{j}})\tilde{v}_j(\mathbf{k})\, d^3\mathbf{x}_0, \tag{A17}$$

$$= (\mathbf{k}\cdot\hat{\mathbf{j}})\tilde{v}_j(\mathbf{k}), \tag{A18}$$

and then identifying $\mathbf{k} \to (\mathbf{k}_0 - \mathbf{k}_2)$, one can rearrange as

$$(\mathbf{k}_0\cdot\hat{\mathbf{j}})\tilde{v}_j(\mathbf{k}_0 - \mathbf{k}_2) = (\mathbf{k}_2\cdot\hat{\mathbf{j}})\tilde{v}_j(\mathbf{k}_0 - \mathbf{k}_2); \tag{A19}$$

this can be substituted this back into Eq. (A14):

$$\frac{1}{2}\partial_t[\tilde{v}_i(\mathbf{k}_2)\tilde{v}_i^*(\mathbf{k}_2)]$$
$$= 2\pi\,\mathrm{Re}\left[\mathrm{i}\int(\mathbf{k}_0\cdot\hat{\mathbf{j}})\tilde{v}_i(\mathbf{k}_2)\tilde{v}_j(\mathbf{k}_0 - \mathbf{k}_2)\tilde{v}_i^*(\mathbf{k}_0)\, d^3\mathbf{k}_0\right]. \tag{A20}$$

Swapping the $\tilde{v}_i$ and noting that the real part of a complex number is invariant under conjugation

$$\frac{1}{2}\partial_t[\tilde{v}_i(\mathbf{k}_2)\tilde{v}_i^*(\mathbf{k}_2)]$$
$$= -2\pi\,\mathrm{Re}\left[\mathrm{i}\int(\mathbf{k}_0\cdot\hat{\mathbf{j}})\tilde{v}_i(\mathbf{k}_0)\tilde{v}_j^*(\mathbf{k}_0 - \mathbf{k}_2)\tilde{v}_i^*(\mathbf{k}_2)\, d^3\mathbf{k}_0\right] \tag{A21}$$

and comparing this with (A12), we can see that energy is indeed conserved, leaving one mode at the same rate it enters another through nonlinear scattering. This is represented graphically in Fig. A2. We stress that for the basic advection term $\partial_t v_i = -v_j\partial_j v_i$, the energy comes entirely from the v_i field on the right-hand side rather than from the v_j field, as one would expect using physical intuition.

Various spectral methods, including spectral fluxes, coarse graining (Aluie et al. 2018), and WTT (e.g., Lvov et al. 2010; Dematteis et al. 2022; Dematteis and Lvov 2021), are sometimes implemented such that scattering is symmetric between the source and catalyst modes. This symmetry between catalyst and source modes is most clearly indicated in the diagrams in Fig. A3. The ideas discussed in this appendix are extended and interpreted in appendix B.

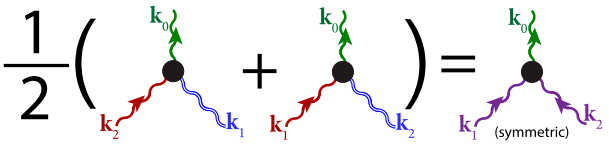

FIG. A3. In some spectral analyses, scattering coefficients are symmetric between the catalyst and source terms. The resulting diagrams can be depicted graphically as in this plot. Diagrams that are symmetric between the source and catalyst modes cannot possess antisymmetry under the exchange of the destination mode with one of the symmetrized modes unless the flow is zero everywhere, meaning information about exchanges of energy between pairs of modes is not directly accessible from such diagrams.

APPENDIX B

Extension to Spectral Frequency Transfers

The spatial spectra transfers discussed in appendix A are often extended to include frequency space without a formal justification or physical interpretation (Arbic et al. 2014; Müller et al. 2015). A more formal derivation and physical interpretation of this decomposition draws on Morten (2015). Following Morten (2015), imagine the kinetic energy (KE) averaged over a window in time of duration T centered at time τ:

$$\langle \mathrm{KE}\rangle = \frac{1}{2TV}\int_{\tau-(T/2)}^{\tau-(T/2)}\int_V v_i(\mathbf{x}, t)v_i(\mathbf{x}, t)\, d^3\mathbf{x}\, dt, \tag{B1}$$

where the angle brackets indicate an average over the spatial domain and the time window and V is the domain volume. This can be expressed as an integral over the spectral decomposition of the velocity field in both wavenumber and frequency:

$$\langle \mathrm{KE}\rangle = \frac{1}{2}\int\int \mathrm{Re}[\hat{\tilde{v}}_i(\mathbf{k}_0, \omega_0, \tau)\hat{\tilde{v}}_i^*(\mathbf{k}_0, \omega_0, \tau)]\, d^3\mathbf{k}\, d\omega, \tag{B2}$$

where the hat (caret) indicates the spectral component in frequency space defined over a window of width T centered at $t = \tau$, the latter of which is considered a free variable,

$$\hat{\tilde{v}}_i(\mathbf{k}, \omega, \tau) = \int_{\tau-(T/2)}^{\tau-(T/2)} \tilde{v}_i(\mathbf{k}, t)e^{2\pi\mathrm{i}\omega t}\, dt. \tag{B3}$$

The KE can be written in terms of components as

$$\langle \mathrm{KE}\rangle(\mathbf{k}_0, \omega_0, \tau) = \frac{1}{2}\mathrm{Re}[\hat{\tilde{v}}_i(\mathbf{k}_0, \omega_0, \tau)\hat{\tilde{v}}_i^*(\mathbf{k}_0, \omega_0, \tau)]. \tag{B4}$$

The change in the KE in the time window centered on τ contributed from $\hat{\tilde{v}}_i(\mathbf{k}_0, \omega_0)$ is then

$$\partial_\tau\langle \mathrm{KE}\rangle(\mathbf{k}_0, \omega_0, \tau) = \mathrm{Re}[\hat{\tilde{v}}_i(\mathbf{k}_0, \omega_0, \tau)\partial_\tau\hat{\tilde{v}}_i(\mathbf{k}_0, \omega, \tau)]. \tag{B5}$$

A key result of Morten (2015) is that (subject to certain constraints on how the velocity field is detrended and tapered), the above is equivalent to

$$\partial_\tau\langle \mathrm{KE}\rangle(\mathbf{k}_0, \omega_0, \tau) = \mathrm{Re}[\hat{\tilde{v}}_i(\mathbf{k}_0, \omega_0, \tau)\widehat{\partial_t\tilde{v}_i^*}(\mathbf{k}_0, \omega_0, \tau)]. \tag{B6}$$

This can then be reworked as

$$\partial_\tau \langle \mathrm{KE} \rangle(\mathbf{k}_0, \omega_0, \tau) = \mathrm{Re}\left\{ \tilde{v}_i(\mathbf{k}_0, \omega_0) \int \partial_t [\tilde{v}_i^*(\mathbf{k}_0, t)] e^{-2\pi \mathrm{i} \omega t} \, dt \right\} \tag{B7}$$

$$= \mathrm{Re}\{\tilde{v}_i(\mathbf{k}_0, \omega_0) \iint -\partial_j [v_j(\mathbf{x}, t) v_i(\mathbf{x}, t)] e^{2\pi \mathrm{i}(\mathbf{k}_0 \cdot \mathbf{x} - \omega_0 t)} \, d^3\mathbf{x} \, dt\} + \mathrm{O.T.}, \tag{B8}$$

where the flux form of the advective term is written out, O.T. refers to the other terms in the momentum equations, and time is integrated from $t = \tau - (T/2)$ to $t = \tau + (T/2)$. Dropping the other terms, one can follow the derivation of KE energy flow from the source to the destination field presented in appendix A with frequencies included and arrive at

$$\partial_\tau \mathrm{KE}(\mathbf{k}_0, \omega_0, \tau) = 2\pi \, \mathrm{Re}\left[\mathrm{i} \iint (\mathbf{k}_0 \cdot \hat{\mathbf{j}}) \tilde{v}_i(\mathbf{k}_0, \omega_0) \tilde{v}_j^* \times (\mathbf{k}_0 - \mathbf{k}_2, \omega_0 - \omega_2) \tilde{v}_i^*(\mathbf{k}_2, \omega_2) \, d^3\mathbf{k}_2 \, d\omega_2 \right]. \tag{B9}$$

Similar to Eq. (A12), Eq. (B9) changes sign under the exchange of $\{\mathbf{k}_0, \omega_0\} \leftrightarrow \{\mathbf{k}_2, \omega_2\}$.

Therefore, the extension of spectral fluxes and transfers to frequency space as used by Arbic et al. (2014) and Müller et al. (2015), as well as in Eqs. (5), (12), (24), and so on, can be interpreted thanks to Morten (2015) as the exchange of energy from a wave of one frequency to another as the sample window over which the frequencies are computed is moved forward in time.

APPENDIX C

Local Spectral Budget

The local spectral KE budget $\mathcal{T}(\mathbf{k}_{\boldsymbol{\alpha}})$ is the evolution of the kinetic energy coming from the spectral components of the velocity fields $\tilde{v}_i(\mathbf{k}_{\boldsymbol{\alpha}})$:

$$\mathcal{T}_{\mathbf{k}_{\boldsymbol{\alpha}}}(t) = \partial_t \mathrm{KE}(t) \tag{C1}$$

$$= V \, \mathrm{Re}[\tilde{v}_{i,\mathbf{k}_{\boldsymbol{\alpha}}}(t) (\widetilde{\partial_t v_i^*})_{\mathbf{k}_{\boldsymbol{\alpha}}}(t)], \tag{C2}$$

where $\mathbf{k}_{\boldsymbol{\alpha}}$ are now discrete wavenumber vectors with mode index vectors $\boldsymbol{\alpha} = \{\alpha_x, \alpha_y, \alpha_z\}$ [defined analogous to the vertical wavenumbers in Eq. (7)], and the tilde notation now refers to a continuous 3D spatial Fourier transform defined on a finite domain of volume V:

$$\tilde{v}_{i,\mathbf{k}_{\boldsymbol{\alpha}}} = \frac{1}{V} \int v_i(\mathbf{x}) e^{-2\pi \mathrm{i}(\mathbf{x} \cdot \mathbf{k}_{\boldsymbol{\alpha}})} \, d^3\mathbf{x}; \quad \mathbf{k}_{\boldsymbol{\alpha}} = \frac{\boldsymbol{\alpha}}{V}; \quad \alpha_i \in \mathbb{Z} \tag{C3}$$

$$v_i(\mathbf{x}) = \sum_{\text{all } \boldsymbol{\alpha}} \tilde{v}_{\mathbf{k}_{\boldsymbol{\alpha}}} e^{2\pi \mathrm{i}(\mathbf{k}_{\boldsymbol{\alpha}} \cdot \mathbf{x})}. \tag{C4}$$

Equation (C2) can then be decomposed into the contributions to the time derivative of the velocity fields coming from the various terms in the spectral momentum equations [which are arrived at by taking the Fourier transform of Eq. (1)]:

$$\mathcal{T}_{\mathrm{term},\mathbf{k}_{\boldsymbol{\alpha}}}(t) = V \, \mathrm{Re}[\tilde{v}_{i,\mathbf{k}_{\boldsymbol{\alpha}}}(t) (\widetilde{\partial_t v_i^*})_{\mathrm{term},\mathbf{k}_{\boldsymbol{\alpha}}}(t)]. \tag{C5}$$

Note that Eqs. (A4)–(A12) refer to the local spectral budget for the advective term, which is referred to as the spectral transfer. Equation (C5) can be computed in position space by writing $\tilde{v}_{i,\mathbf{k}_{\boldsymbol{\alpha}}}(t)$ as a sinusoidal function:[C1]

$$\mathcal{T}_{\mathrm{term},\mathbf{k}_{\boldsymbol{\alpha}}}(t) = \frac{1}{2} \int \sum_{\boldsymbol{\gamma} = \pm \boldsymbol{\alpha}} \tilde{v}_{i,\mathbf{k}_{\boldsymbol{\gamma}}}(t) e^{2\pi \mathrm{i}(\mathbf{k}_{\boldsymbol{\gamma}} \cdot \mathbf{x})} \partial_t v_{i,\mathrm{term}}(\mathbf{x}, t) \, d^3\mathbf{x}, \tag{C6}$$

where V is the volume over which the spectral components are defined, the time derivative of the velocity field is not decomposed into spectral components. If we note that $\mathcal{T}_{\mathrm{term},\mathbf{k}_{\boldsymbol{\alpha}}}(t)$ is invariant under $\mathbf{k}_{\boldsymbol{\alpha}} \leftrightarrow -\mathbf{k}_{\boldsymbol{\alpha}}$, then in one dimension it can be useful to remove the factor of 1/2 and restrict the wavenumber argument of $\mathrm{T}_{\mathrm{term}}$ to be positive, as is done in the body of this paper for vertical wavenumbers m defined along the vertical spatial coordinate z.

$$\mathcal{T}_{\mathrm{term},|m_\alpha|}(t) = \int \sum_{\gamma = \pm \alpha} \tilde{v}_{i,m_\gamma}(t) e^{2\pi \mathrm{i} m_\gamma z} \partial_t v_{i,\mathrm{term}}(z, t) \, dz. \tag{C7}$$

The extension of Eq. (C6) to include frequency as well as wavenumber given in Eq. (5) can be derived by starting with Eq. (B6). To do this, we must now define the local spectral budget as the change in KE from a given mode, $\{\mathbf{k}_{\boldsymbol{\alpha}}, \omega_{\boldsymbol{\alpha}}\}$, defined over a window in time of duration T centered at time $t = \tau$ that moves forward with time, as described in appendix B:

$$\mathcal{T}_{\mathrm{term},\mathbf{k}_{\boldsymbol{\alpha}},\omega_\beta}(\tau) = \partial_\tau \mathrm{KE}_{\mathbf{k}_{\boldsymbol{\alpha}},\omega_\beta}(\tau) \tag{C8}$$

$$= VT \, \mathrm{Re}[\hat{\tilde{v}}_{i,\mathbf{k}_{\boldsymbol{\alpha}},\omega_\beta}(\tau) (\widetilde{\widetilde{\partial_t v_i^*}})_{\mathrm{term},\mathbf{k}_{\boldsymbol{\alpha}},\omega_\beta}(\tau)]. \tag{C9}$$

Here, the tilde–hat indicates Fourier amplitudes in both frequency and wavenumber [Eq. (B3)] and Eq. (C9) follows from Eq. (C8) by Eq. (B6). Then, the velocity evolution can be decomposed into the budget contributions from individual terms and expressed as an integral of a sinusoid over position and time:

[C1] For a derivation of this point, consider generic discrete spectral functions $\tilde{g}_{\mathbf{k}_\alpha}$ and $\tilde{h}_{\mathbf{k}_\beta}$ and their continuous spatial counterparts $g(\mathbf{x})$ and $h(\mathbf{x})$:

$$\begin{aligned}
\frac{1}{2} \int \sum_{\gamma = \pm \alpha} \tilde{g}_{\mathbf{k}_\gamma} e^{2\pi \mathrm{i}(\mathbf{k}_\gamma \cdot \mathbf{x})} h(\mathbf{x}) \, d^3\mathbf{x} &= \frac{1}{2} \int \sum_{\gamma = \pm \alpha} \tilde{g}_{\mathbf{k}_\gamma} e^{2\pi \mathrm{i}(\mathbf{k}_\gamma \cdot \mathbf{x})} [\sum_{\text{all } \lambda} \tilde{h}_{\mathbf{k}_\lambda} e^{2\pi \mathrm{i}(\mathbf{k}_\lambda \cdot \mathbf{x})}] \, d^3\mathbf{x} \\
&= \frac{1}{2} \int \sum_{\substack{\gamma = \pm \alpha \\ \text{all } \lambda}} e^{2\pi \mathrm{i}[(\mathbf{k}_\gamma + \mathbf{k}_\lambda) \cdot \mathbf{x}]} \tilde{g}_{\mathbf{k}_\gamma} \tilde{h}_{\mathbf{k}_\lambda} \, d^3\mathbf{x} \\
&= \frac{1}{2} \int \sum_{\substack{\gamma = \pm \alpha \\ \text{all } \lambda}} e^{2\pi \mathrm{i}[(\mathbf{k}_\gamma + \mathbf{k}_\lambda) \cdot \mathbf{x}]} \tilde{g}_{\mathbf{k}_\gamma} \tilde{h}_{\mathbf{k}_\lambda} \, d^3\mathbf{x} \\
&= \frac{1}{2} \sum_{\substack{\gamma = \pm \alpha \\ \text{all } \lambda}} V \delta^3_{\mathbf{k}_\gamma, -\mathbf{k}_\lambda} \tilde{g}_{\mathbf{k}_\gamma} \tilde{h}_{\mathbf{k}_\lambda} \\
&= \frac{V}{2} \sum_{\text{all } \lambda} (\delta^3_{\mathbf{k}_\alpha, -\mathbf{k}_\lambda} \tilde{g}_{\mathbf{k}\alpha} \tilde{h}_{\mathbf{k}_\lambda} + \delta^3_{\mathbf{k}_\alpha, \mathbf{k}_\lambda} \tilde{g}_{-\mathbf{k}_\alpha} \tilde{h}_{\mathbf{k}_\lambda}) \\
&= \frac{V}{2} \tilde{g}_{\mathbf{k}_\alpha} \tilde{h}_{-\mathbf{k}_\alpha} + \frac{V}{2} \tilde{g}_{-\mathbf{k}_\alpha} \tilde{h}_{\mathbf{k}_\alpha} = V \, \mathrm{Re}(\tilde{g}_{\mathbf{k}_\alpha} \tilde{h}_{-\mathbf{k}_\alpha}),
\end{aligned}$$

where integration is over a domain of volume V and δ^3 is the three-dimensional Kronecker delta.

$$\mathcal{T}_{\text{term},\mathbf{k}_\alpha,\omega_\beta}(\tau) = \frac{1}{2}\iint \sum_{\substack{\boldsymbol{\gamma}=\pm\boldsymbol{\alpha}\\ \lambda=\pm\beta}} \hat{v}_{i,\mathbf{k}_\gamma,\omega_\lambda}(\tau) e^{2\pi \mathrm{i}(\mathbf{k}_\gamma\cdot\mathbf{x}-\omega_\lambda t)} \times \partial_t v_{i,\text{term}}(\mathbf{x}, t)\, dt\, d^3\mathbf{x}, \tag{C10}$$

Similar to Eq. (C7), Eq. (C10) can be written as a function of positive m_α:

$$\mathcal{T}_{\text{term},|m_\alpha|,\omega_\beta}(\tau) = \iint \sum_{\substack{\gamma=\pm\alpha\\ \lambda=\pm\beta}} \hat{v}_{i,m_\gamma,\omega_\lambda}(\tau) e^{2\pi \mathrm{i}(m_\gamma z-\omega_\lambda t)} \times \partial_t v_{i,\text{term}}(\mathbf{x}, t)\, dt\, dz. \tag{C11}$$

Under the hydrostatic approximation and as is done in this paper, it is useful to define $\mathrm{KE}_{\text{hyd}} = u_i u_i = u_1^2 + u_2^2$, which is conserved under the action of the hydrostatic advective operator in the bulk of fluid. In this case, indices on u only sum over the two horizontal dimensions and the vertical spectral transfer is

$$\mathcal{T}_{\text{hyd,term},|m_\alpha|,\omega_\beta}(\tau) = \iint \sum_{\substack{\gamma=\pm\alpha\\ \lambda=\pm\beta}} \hat{u}_{i,m_\gamma,\omega_\lambda}(\tau) e^{2\pi \mathrm{i}(m_\gamma z-\omega_\lambda t)} \times \partial_t u_{i,\text{term}}(\mathbf{x}, t)\, dt\, dz. \tag{C12}$$

The hydrostatic label will be dropped in the body of this paper.

APPENDIX D

Divergence Correction

This appendix is mentioned in appendix E. To handle the horizontal boundaries in computing spectral transfers and fluxes from the advective term, the flow field is assumed to be periodic and the resulting divergence is explicitly removed:

$$\Pi^{>}_{\text{LP}\xrightarrow{\text{BP}}\text{HP},m_\alpha} = -\left\langle \iint \sum_{\substack{|\gamma|>|\alpha|\\ \text{all }\lambda}} \hat{u}^{\text{HP}}_{i,m_\gamma,\omega_\lambda}(x, y) e^{2\pi \mathrm{i}(m_\gamma z-\omega_\lambda t)} (v_j \partial_j u_i)\, dz\, dt \right\rangle + \frac{1}{2}\left\langle \iint \sum_{\substack{|\gamma|>|\alpha|\\ \text{all }\lambda}} \hat{u}^{\text{HP}}_{i,m_\gamma,\omega_\lambda}(x, y) u_i(\partial_j v_j)\, dz\, dt \right\rangle. \tag{D1}$$

This procedure forces the spectral flux to conserve energy within the domain (up to discretization and interpolation error) and has the added benefit of correctly handling the advective flux associated with the free surface of the flow. The procedure does introduce error from the sharp gradients imposed at the periodic boundaries, but this error is deemed to be a worthwhile sacrifice to conserve energy under the advective operator. This procedure was not used for the calculation of wavenumber–frequency transfers because energy conservation was not so important in this context as to merit the expense of implementing and computing this correction.

APPENDIX E

Budget Term Diagnosis Implementation

Below are details of the numerical methods used to diagnose various terms in the spectral budgets used in this paper. Also, see Adcroft et al. (2015) and Nelson et al. (2020) for further information on the solver details and simulation settings.

- Advection (A) is a flux form centered second-order operator. In our analysis, we compute this term exactly as in the model, except that it is computed on a vertically uniform grid. Experiments suggest that this procedure yields better energy conservation than interpolation after the velocity tendencies are computed. All other terms are computed on the nonuniform grid and then interpolated. Horizontal boundary conditions are handled by assuming periodicity and explicitly removing the energy sources/sinks associated with the resulting unphysical (three dimensional) flow divergence, as described in appendix D.
- Advection of kinetic energy into the simulation domain from the boundaries (BCs) is computed explicitly at the surfaces of the region being analyzed. This is done with the same flux-form discretization as for the previously mentioned volume advection operator.
- KPP background and shear ($\mathsf{D}_{\text{KPP\_BG}}$ and $\mathsf{D}_{\text{KPP\_Shear}}$) are computed using the same discretizations as in the model below 20 m depth, using a 30-m one-sided Tukey taper from 20 to 50 m. The taper excludes the vast majority of the diagnosed mixed layer, which always lies within the upper 50 m during the weeklong model output period across the domain. The mixed layer dissipation ($\mathsf{D}_{\text{KPP\_ML}}$) is entirely omitted in the hope that it will prove to be unimportant in the general balance of the IW field and any other conclusions drawn from this work. The findings of this work generally support this assumption. All other terms are computed throughout the entirety of the water column.
- The Leith scheme ($\mathsf{D}_{\text{Leith}}$) is computed using the same discretizations as in the model.
- Quadratic bottom boundary layer drag (D_{QBD}) is computed exactly as it is in the model. This term implicitly handles the no-slip bottom boundary condition.
- A no-slip side boundary condition is computed exactly as it is computed in the model (BCs). This contribution was found to be negligible and is therefore omitted from the results.
- Bottom scattering and the pressure boundary condition (i.e., the no-normal flow condition, BCs) are handled implicitly in the other terms, such as advection.
- The pressure term (P) mediates the linear transfer of potential energy into kinetic energy via the hydrostatic pressure but will not transfer kinetic energy among scales away from the boundary conditions. This potential-energy-to-kinetic-energy conversion was computed through the pressure in a manner that is a good approximation of how it is represented in the model. The conversion turns out to not have a significant

impact for higher vertical wavenumbers and is not included in any budget plots.

- The Coriolis force (C) rotates the modes containing KE but, as a linear term, does not transfer it among scales. Thus the Coriolis term is not computed for spectral budgets in this paper. The contribution to the drag from the scattering of the Coriolis tendency off of the bottom topography is not computed but has been determined to be very small in a different test case.
- In some figures, the total energy dissipation is given. This total dissipation is the sum of dissipations associated with the KPP background and shear terms, the Leith scheme, and quadratic bottom drag, but omits the KPP mixed layer term.
- Last, a residual is computed as the sum of the aforementioned terms. The residual includes the combined interpolation and discretization errors of each term, any omitted forcing, the KPP mixed layer dissipation, the small contributions of intentionally neglected terms that were previously mentioned, as well as energy buildup over time.

The KE budget terms are computed across the entirety of the water column (with the exception of KPP) in part because the flow is vertically inhomogeneous. In terms of spectral analysis, the flow resembles a transient signal in position space, and it is appropriate to use a rectangular taper function (i.e., no taper function) to capture parts of the signal at the top and bottom of the domain. Put another way, no taper is needed for this analysis because the analysis does not compute the spectrum from a sample of an infinite dimension. Rather, the spectrum is computed on the entire domain on which the signal is defined. The exception to this, as previously mentioned, is KPP's interior dissipation, which tapered from 20 to 50 m while KPP's mixed layer dissipation is simply omitted. Also note that a Tukey taper is applied in time.

APPENDIX F

Definitions of Scale-Separated Interactions

The scale-separation factor ξ is introduced in Eq. (14) to identify triads with two modes that are much larger in vertical wavenumber that the third. The breakdown of energy in $\Pi^{>}_{\mathrm{HP}\xrightarrow{\mathrm{BP}}\mathrm{HP}}$ between $\Pi^{>}_{\mathrm{ID}_{\mathrm{diff}}}$ and $\Pi^{>}_{\mathrm{LI}}$ as a function of vertical wavenumber m and scale-separation factor ξ is depicted in Figure F1. The breakdown is strongly dependent on wavenumber, with a greater portion of the spectral flux being attributed to $\mathrm{ID}_{\mathrm{diff}}$ at higher vertical wavenumber, as well as the scale separation factor. Given the small amount of diagnosed $\Pi^{>}_{\mathrm{ID}_{\mathrm{diff}}}$ (see section 3), its tendency to increase with vertical wavenumber and resolution (see section 3) as well as the need to see how $\Pi^{>}_{\mathrm{ID}_{\mathrm{diff}}}$ varies regionally and with resolution in the model output, we choose a less restrictive definition of scale separation of $\xi = 2$ as compared with those commonly used in idealized models where greater resolution is available (Dematteis et al. 2022).

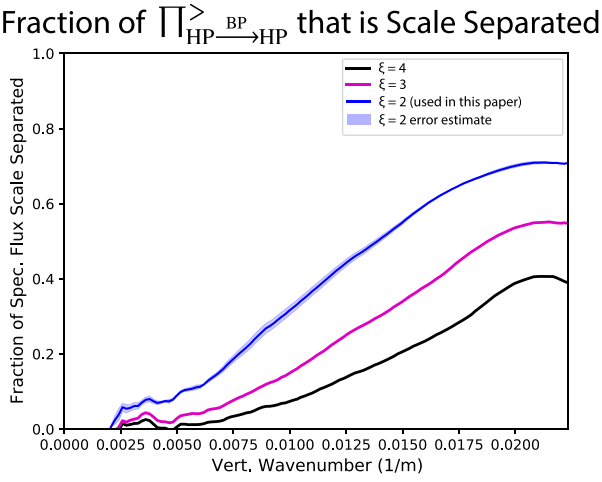

FIG. F1. The fraction of $\Pi^{>}_{\mathrm{HP}\xrightarrow{\mathrm{BP}}\mathrm{HP}}$ that is scale separated as based on different definitions of scale separation. These scale separations can be most clearly visualized in the bispectra introduced in section 3; see Figs. 8a, 11d, and 11b.

Figure F1 also shows an estimate[F1] of the error introduced by our approximate definition of scale separation for $\Pi^{>}_{\mathrm{BP}\xrightarrow{\mathrm{HP}}\mathrm{HP}}$, which is found to be less than 10% for destination wavenumbers greater than 3.4 cycles per kilometer. Error in the decomposition of $\Pi^{>}_{\mathrm{BP}\xrightarrow{\mathrm{HP}}\mathrm{HP}}$ is found using a similar method to be less than 20% for destination wavenumbers greater than 4.0 cycles per kilometer (not shown). The partition of spectral fluxes into scale-separated and local components is visualized with the dotted lines in the bispectra presented in section 3b. The $\Pi^{>}_{\mathrm{HP}\xrightarrow{\mathrm{BP}}\mathrm{HP}}$ is shown in Fig. 8a while the breakdown of $\Pi^{>}_{\mathrm{BP}\xrightarrow{\mathrm{HP}}\mathrm{HP}}$ is visualized in Fig. 11b and to a poorer approximation in Fig. 8d.

[F1] The error introduced by defining scale separation in $\Pi^{>}_{\mathrm{BP}\xrightarrow{\mathrm{HP}}\mathrm{HP}}$ as modes with $\min(|m_{\mathrm{src}}|, |m_{\mathrm{dest}}|)/(|m_{\mathrm{src}}| - |m_{\mathrm{dest}}|) < \xi$ instead of exactly as modes with $\min(|m_{\mathrm{src}}|, |m_{\mathrm{dest}}|)/(|m_{\mathrm{src}} - m_{\mathrm{dest}}|) < \xi$ is estimated by decomposing the spectral flux into source–destination bispectral components [$\mathcal{B}_{\mathbf{HP}\xrightarrow{\mathrm{BP}}\mathbf{HP},|m_{\mathrm{src}}|,|m_{\mathrm{dest}}|}$; Eq. (25)] and then mapping each component to the two associated realizations of the catalyst–destination bispectral components [$\mathcal{B}_{\mathrm{HP}\xrightarrow{\mathrm{BP}}\mathbf{HP},|m^{\mathrm{cat}}_{\alpha}|,|m^{\mathrm{dest}}_{\alpha}|}$; Eq. (24)]. One realization, $|m_{\mathrm{cat}}| = |m_{\mathrm{dest}}| - |m_{\mathrm{src}}|$, is associated with the actual scale-separated signal. The other realization, $|m_{\mathrm{cat}}| = |m_{\mathrm{dest}}| + |m_{\mathrm{src}}|$, is associated with an erroneous signal with a very large catalyst mode. The ratio of these two realizations is used to compute the error. This is not a perfect measure of the error as the catalyst-destination bispectra also have two different realizations in the source–destination bispectra; however, given the rapid fall off of such spectral transfers with catalyst wavenumber (the desired realization typically has an order-of-magnitude greater signal than the erroneous realization), it is a good estimate. This type of bispectral analysis shows promise for making higher-order corrections to estimates of scale-separated interactions in future work.

REFERENCES

Adcroft, A., and Coauthors, 2015: MITgcm user's manual. Dept. of Earth, Atmospheric and Planetary Sciences, Massachusetts Institute of Technology, https://mitgcm.readthedocs.io/en/latest/.

Alford, M. H., J. MacKinnon, Z. Zhao, R. Pinkel, J. Klymak, and T. Peacock, 2007: Internal waves across the pacific. *Geophys. Res. Lett.*, **34**, L24601, https://doi.org/10.1029/2007GL031566.

——, J. A. MacKinnon, R. Pinkel, and J. M. Klymak, 2017: Space–time scales of shear in the North Pacific. *J. Phys. Oceanogr.*, **47**, 2455–2478, https://doi.org/10.1175/JPO-D-17-0087.1.

Aluie, H., M. Hecht, and G. K. Vallis, 2018: Mapping the energy cascade in the North Atlantic Ocean: The coarse-graining approach. *J. Phys. Oceanogr.*, **48**, 225–244, https://doi.org/10.1175/JPO-D-17-0100.1.

Arbic, B. K., 2022: Incorporating tides and internal gravity waves within global ocean general circulation models: A review. *Prog. Oceanogr.*, **206**, 102824, https://doi.org/10.1016/j.pocean.2022.102824.

——, A. J. Wallcraft, and E. J. Metzger, 2010: Concurrent simulation of the eddying general circulation and tides in a global ocean model. *Ocean Modell.*, **32**, 175–187, https://doi.org/10.1016/j.ocemod.2010.01.007.

——, K. L. Polzin, R. B. Scott, J. G. Richman, and J. F. Shriver, 2013: On eddy viscosity, energy cascades, and the horizontal resolution of gridded satellite altimeter products. *J. Phys. Oceanogr.*, **43**, 283–300, https://doi.org/10.1175/JPO-D-11-0240.1.

——, M. Müller, J. G. Richman, J. F. Shriver, A. J. Morten, R. B. Scott, G. Sérazin, and T. Penduff, 2014: Geostrophic turbulence in the frequency–wavenumber domain: Eddy-driven low-frequency variability. *J. Phys. Oceanogr.*, **44**, 2050–2069, https://doi.org/10.1175/JPO-D-13-054.1.

——, and Coauthors, 2018: A primer on global internal tide and internal gravity wave continuum modeling in HYCOM and MITgcm. *New Frontiers in Operational Oceanography*, GODAE OceanView, 307–392, https://doi.org/10.17125/gov2018.ch13.

Capet, X., J. C. McWilliams, M. J. Molemaker, and A. F. Shchepetkin, 2008: Mesoscale to submesoscale transition in the California Current System. Part I: Flow structure, eddy flux, and observational tests. *J. Phys. Oceanogr.*, **38**, 29–43, https://doi.org/10.1175/2007JPO3671.1.

Delpech, A., R. Barkan, L. Renault, J. McWilliams, O. Q. Siyanbola, M. C. Buijsman, and B. K. Arbic, 2023: Wind-current feedback is an energy sink for oceanic internal waves. *Sci. Rep.*, **13**, 5915, https://doi.org/10.1038/s41598-023-32909-6.

Dematteis, G., and Y. V. Lvov, 2021: Downscale energy fluxes in scale-invariant oceanic internal wave turbulence. *J. Fluid Mech.*, **915**, A129, https://doi.org/10.1017/jfm.2021.99.

——, and ——, 2023: The structure of energy fluxes in wave turbulence. *J. Fluid Mech.*, **954**, A30, https://doi.org/10.1017/jfm.2022.995.

——, K. Polzin, and Y. V. Lvov, 2022: On the origins of the oceanic ultraviolet catastrophe. *J. Phys. Oceanogr.*, **52**, 597–616, https://doi.org/10.1175/JPO-D-21-0121.1.

Dong, W., O. Bühler, and K. S. Smith, 2020: Frequency diffusion of waves by unsteady flows. *J. Fluid Mech.*, **905**, R3, https://doi.org/10.1017/jfm.2020.837.

Eden, C., and D. Olbers, 2014: An energy compartment model for propagation, nonlinear interaction, and dissipation of internal gravity waves. *J. Phys. Oceanogr.*, **44**, 2093–2106, https://doi.org/10.1175/JPO-D-13-0224.1.

——, F. Pollmann, and D. Olbers, 2020: Towards a global spectral energy budget for internal gravity waves in the ocean. *J. Phys. Oceanogr.*, **50**, 935–944, https://doi.org/10.1175/JPO-D-19-0022.1.

Fox-Kemper, B., and D. Menemenlis, 2008: Can large eddy simulation techniques improve mesoscale rich ocean models? *Ocean Modeling in an Eddying Regime*, *Geophys. Monogr.*, Vol. 177, Amer. Geophys. Union, 319–337, https://doi.org/10.1029/177GM19.

Frisch, U., and A. N. Kolmogorov, 1995: *Turbulence: The Legacy of AN Kolmogorov*. Cambridge University Press, 296 pp.

Gargett, A. E., and G. Holloway, 1984: Dissipation and diffusion by internal wave breaking. *J. Mar. Res.*, **42**, 15–27, https://doi.org/10.1357/002224084788506158.

Garrett, C., and W. Munk, 1972: Space-time scales of internal waves. *Geophys. Fluid Dyn.*, **3**, 225–264, https://doi.org/10.1080/03091927208236082.

——, and ——, 1975: Space-time scales of internal waves: A progress report. *J. Geophys. Res.*, **80**, 291–297, https://doi.org/10.1029/JC080i003p00291.

——, and ——, 1979: Internal waves in the ocean. *Annu. Rev. Fluid Mech.*, **11**, 339–369, https://doi.org/10.1146/annurev.fl.11.010179.002011.

IPCC, 2013: *Climate Change 2013: The Physical Science Basis*. T. F. Stocker et al., Eds., Cambridge University Press, 1535 pp.

Large, W. G., J. C. McWilliams, and S. C. Doney, 1994: Oceanic vertical mixing: A review and a model with a nonlocal boundary layer parameterization. *Rev. Geophys.*, **32**, 363–403, https://doi.org/10.1029/94RG01872.

Lvov, Y. V., K. L. Polzin, E. G. Tabak, and N. Yokoyama, 2010: Oceanic internal-wave field: Theory of scale-invariant spectra. *J. Phys. Oceanogr.*, **40**, 2605–2623, https://doi.org/10.1175/2010JPO4132.1.

Marston, J., G. Chini, and S. Tobias, 2016: Generalized quasilinear approximation: Application to zonal jets. *Phys. Rev. Lett.*, **116**, 214501, https://doi.org/10.1103/PhysRevLett.116.214501.

Mazloff, M. R., B. Cornuelle, S. T. Gille, and J. Wang, 2020: The importance of remote forcing for regional modeling of internal waves. *J. Geophys. Res. Oceans*, **125**, e2019JC015623, https://doi.org/10.1029/2019JC015623.

McComas, C. H., 1977: Equilibrium mechanisms within the oceanic internal wave field. *J. Phys. Oceanogr.*, **7**, 836–845, https://doi.org/10.1175/1520-0485(1977)007<0836:EMWTOI>2.0.CO;2.

——, and F. P. Bretherton, 1977: Resonant interaction of oceanic internal waves. *J. Geophys. Res.*, **82**, 1397–1412, https://doi.org/10.1029/JC082i009p01397.

——, and P. Müller, 1981: The dynamic balance of internal waves. *J. Phys. Oceanogr.*, **11**, 970–986, https://doi.org/10.1175/1520-0485(1981)011<0970:TDBOIW>2.0.CO;2.

Morten, A. J., 2015: Spatio-temporal spectra and spectral transfers in fluid dynamics. Ph.D. thesis, University of Michigan, 146 pp.

Müller, M., B. K. Arbic, J. G. Richman, J. F. Shriver, E. L. Kunze, R. B. Scott, A. J. Wallcraft, and L. Zamudio, 2015: Toward an internal gravity wave spectrum in global ocean models. *Geophys. Res. Lett.*, **42**, 3474–3481, https://doi.org/10.1002/2015GL063365.

Müller, P., G. Holloway, F. Henyey, and N. Pomphrey, 1986: Nonlinear interactions among internal gravity waves. *Rev. Geophys.*, **24**, 493–536, https://doi.org/10.1029/RG024i003p00493.

Nelson, A., B. Arbic, D. Menemenlis, W. Peltier, M. Alford, N. Grisouard, and J. Klymak, 2020: Improved internal wave spectral continuum in a regional ocean model. *J. Geophys. Res. Oceans*, **125**, e2019JC015974, https://doi.org/10.1029/2019JC015974.

Nugroho, D., A. Koch-Larrouy, P. Gaspar, F. Lyard, G. Reffray, and B. Tranchant, 2018: Modelling explicit tides in the Indonesian seas: An important process for surface sea water properties. *Mar. Pollut. Bull.*, **131**, 7–18, https://doi.org/10.1016/j.marpolbul.2017.06.033.

Olbers, D. J., 1976: Nonlinear energy transfer and the energy balance of the internal wave field in the deep ocean. *J. Fluid Mech.*, **74**, 375–399, https://doi.org/10.1017/S0022112076001857.

——, and C. Eden, 2013: A global model for the diapycnal diffusivity induced by internal gravity waves. *J. Phys. Oceanogr.*, **43**, 1759–1779, https://doi.org/10.1175/JPO-D-12-0207.1.

Pan, Y., B. K. Arbic, A. D. Nelson, D. Menemenlis, W. Peltier, W. Xu, and Y. Li, 2020: Numerical investigation of mechanisms underlying oceanic internal gravity wave power-law spectra. *J. Phys. Oceanogr.*, **50**, 2713–2733, https://doi.org/10.1175/JPO-D-20-0039.1.

Polzin, K. L., and Y. V. Lvov, 2017: An oceanic ultra-violet catastrophe, wave-particle duality and a strongly nonlinear concept for geophysical turbulence. *Fluids*, **2**, 36, https://doi.org/10.3390/fluids2030036.

Renault, L., J. C. McWilliams, F. Kessouri, A. Jousse, H. Frenzel, R. Chen, and C. Deutsch, 2021: Evaluation of high-resolution atmospheric and oceanic simulations of the California Current system. *Prog. Oceanogr.*, **195**, 102564, https://doi.org/10.1016/j.pocean.2021.102564.

Rocha, C. B., T. K. Chereskin, S. T. Gille, and D. Menemenlis, 2016a: Mesoscale to submesoscale wavenumber spectra in Drake Passage. *J. Phys. Oceanogr.*, **46**, 601–620, https://doi.org/10.1175/JPO-D-15-0087.1.

——, S. T. Gille, T. K. Chereskin, and D. Menemenlis, 2016b: Seasonality of submesoscale dynamics in the Kuroshio Extension. *Geophys. Res. Lett.*, **43**, 11 304–11 311, https://doi.org/10.1002/2016GL071349.

Savage, A. C., and Coauthors, 2017: Spectral decomposition of internal gravity wave sea surface height in global models. *J. Geophys. Res. Oceans*, **122**, 7803–7821, https://doi.org/10.1002/2017JC013009.

Savva, M. A., and J. Vanneste, 2018: Scattering of internal tides by barotropic quasigeostrophic flows. *J. Fluid Mech.*, **856**, 504–530, https://doi.org/10.1017/jfm.2018.694.

Schlösser, F., and C. Eden, 2007: Diagnosing the energy cascade in a model of the North Atlantic. *Geophys. Res. Lett.*, **34**, L02604, https://doi.org/10.1029/2006GL027813.

Scott, R. B., and F. Wang, 2005: Direct evidence of an oceanic inverse kinetic energy cascade from satellite altimetry. *J. Phys. Oceanogr.*, **35**, 1650–1666, https://doi.org/10.1175/JPO2771.1.

——, and B. K. Arbic, 2007: Spectral energy fluxes in geostrophic turbulence: Implications for ocean energetics. *J. Phys. Oceanogr.*, **37**, 673–688, https://doi.org/10.1175/JPO3027.1.

Siyanbola, O. Q., M. C. Buijsman, A. Delpech, L. Renault, R. Barkan, J. F. Shriver, B. K. Arbic, and J. C. McWilliams, 2023: Remote internal wave forcing of regional ocean simulations near the US West Coast. *Ocean Modell.*, **181**, 102154, https://doi.org/10.1016/j.ocemod.2022.102154.

Skitka, J., and Coauthors, 2022: Data repository for probing the nonlinear interactions of supertidal internal waves using a high-resolution regional ocean model. Harvard Dataverse, https://doi.org/10.7910/DVN/FSMM1O.

Sun, O. M., and R. Pinkel, 2012: Energy transfer from high-shear, low-frequency internal waves to high-frequency waves near Kaena Ridge, Hawaii. *J. Phys. Oceanogr.*, **42**, 1524–1547, https://doi.org/10.1175/JPO-D-11-0117.1.

Thakur, R., and Coauthors, 2022: Impact of vertical mixing parameterizations on internal gravity wave spectra in regional ocean models. *Geophys. Res. Lett.*, **49**, e2022GL099614, https://doi.org/10.1029/2022GL099614.

Wagner, G., and W. Young, 2016: A three-component model for the coupled evolution of near-inertial waves, quasi-geostrophic flow and the near-inertial second harmonic. *J. Fluid Mech.*, **802**, 806–837, https://doi.org/10.1017/jfm.2016.487.

Wang, Y., Z. Xu, T. Hibiya, B. Yin, and F. Wang, 2021: Radiation path of diurnal internal tides in the northwestern Pacific controlled by refraction and interference. *J. Geophys. Res. Oceans*, **126**, e2020JC016972, https://doi.org/10.1029/2020JC016972.

Wunsch, C., and R. Ferrari, 2004: Vertical mixing, energy, and the general circulation of the oceans. *Annu. Rev. Fluid Mech.*, **36**, 281–314, https://doi.org/10.1146/annurev.fluid.36.050802.122121.